
STRUCTURE, PHASE TRANSFORMATIONS,
AND DIFFUSION

Simulation of Microstructure Evolution in Metal Materials under Hot Plastic Deformation and Heat Treatment

A. Yu. Churyumov^{a, *} and A. V. Pozdniakov^a

^aNational University of Science and Technology MISiS, Moscow, 119991 Russia

*e-mail: churyumov@misis.ru

Received April 1, 2020; revised July 4, 2020; accepted July 14, 2020

Abstract—The development of modern computational techniques and equipment enables one to perform high-precision calculations of complex processes for industry, including metallurgy. This review has classified the basic physical and mathematical models of structure formation during heat and deformation treatment. The Kocks–Mecking–Estrin model describing the dislocation structure at the initial stage of hot plastic deformation has been analyzed. The models of dynamic, metadynamic, and static recrystallization kinetics based on the Johnson–Mehl–Avrami–Kolmogorov equation have been considered. The models of the kinetics of phase transformation upon heating and cooling of steel have been reviewed. The Kampmann–Wagner model that describes the decomposition of supersaturated solid solution during the aging of aluminum alloys has also been considered. The main computational techniques to calculate microstructural evolution, such as the cellular automaton, Monte Carlo, and multiphase-field techniques have been considered. They exhibit high accuracy when calculating recrystallization processes and phase transformations. The systematization of the existing models that describe structural evolution has revealed the possibility to develop complex models for the comprehensive calculation of full cycles to process metal materials by heating and deformation. These models can be used for the optimization and development of new processing techniques.

Keywords: simulation, structure, Johnson–Mehl–Avrami–Kolmogorov model, recrystallization, computational techniques

DOI: 10.1134/S0031918X20110034

CONTENT

INTRODUCTION

1. SIMULATION OF THE STRUCTURAL EVOLUTION UNDER HOT PLASTIC DEFORMATION

- 1.1. Dynamic strain hardening and recovery
- 1.2. Dynamic recrystallization
- 1.3. Metadynamic recrystallization
- 1.4. Static recrystallization
- 1.5. Grain growth during annealing

2. SIMULATION OF PHASE TRANSFORMATION KINETICS IN STEELS

- 2.1. Austenite formation during heating
- 2.2. Processes of austenite transformation during cooling

3. SIMULATION OF THE STRUCTURAL EVOLUTION DURING SUPERSATURATED SOLID SOLUTION DECOMPOSITION

4. COMPUTATIONAL METHODS FOR CALCULATING STRUCTURAL EVOLUTION

- 4.1. Cellular automaton method
- 4.2. Monte Carlo method

4.3. Multiphase-field method CONCLUSIONS

INTRODUCTION

The development of modern computational techniques and equipment enables one to perform high-precision calculations of complex processes for industry, including metallurgy. The specific microstructure and the corresponding level of properties are the main factors that determine the quality of commercial metallurgical products. The microstructure in metal materials forms primarily during the final stages of metallurgical processing, namely, deformation and heat treatment. Developing a systematic database of physical and mathematical models describing microstructure formation during plastic deformation and heat treatment is therefore an urgent task.

The models associating microstructural parameters (volume fraction, recrystallized-grain size) with deformation parameters, which are described by Avrami–Kolmogorov-type equations, are currently the most widespread for modeling structural evolution under hot plastic deformation. They show high predictive accuracy, although they require a large amount

of experimental data to determine unknown constants. Initially, mathematical equations relating the microstructural parameters with thermo-deformation ones were employed for high-temperature alloys like Waspalloy [1] and Inconel [2] and were later used for a wider range of metal materials. However, models based on such equations can predict microstructure parameters only for alloys that are deformed in a single-phase region. The Avrami–Kolmogorov-type equations should be supplemented with equations describing phase transformations for the alloys in which hot plastic deformation initiates phase transformations. Identifying constants of these equations for specific materials requires additional dilatometric and microstructural studies, as well as complex calculations [3–6]. However, it significantly extends the possibilities of predicting the structure in materials after multistage deformation and heat treatment. These models are developed for low-carbon [7, 8] and hyper-eutectoid chrome-bearing steels [9]. In addition, particular attention should be paid to the mathematical characterization of the supersaturated solid solution decomposition, resulting in the formation of the metastable modifications of hardening phases (aging products in aluminum alloys, carbide and carbonitride phases in steels [10, 11], and others), because they have a significant effect on the final properties of products.

Computational methods, such as cellular automaton, are alternative methods of modeling the structure formation. This method involves dividing the region under study into separate elements (cells) whose state is determined not only by external factors (temperature, strain rate, degree of accumulated deformation) but also by the state of neighboring cells. The calculation results in a complete picture of the evolution of structural parameters in the simulated region of the material during the whole process of deformation and heat treatment. Despite the large volume of structural studies required for accurate calculation, this method is promising for structure modeling in modern materials science, which is evidenced by the large number of publications devoted to it. The cellular automaton method was used to simulate structural evolution in an AISI 304L steel [12], to describe dynamic recrystallization in a 42CrMo steel [13], to describe phase transformations in two phase steel upon heating, and to simulate other processes of structural formation during deformation and heat treatment.

The aim of this review article is to systematize modern physical and mathematical models and computational methods simulating the structural evolution. This systematization enables one to create a theoretical foundation for the development of smart technologies of plastic deformation and thermal treatment of metallic materials. A simplified algorithm for calculating and controlling the microstructural parameters of metal materials during thermal and deformation processing is shown in Fig. 1. Algorithmization of

physical-mathematical and computation models allows using them together with the methods of finite element modeling, which is time and cost-effective for the optimization of existing and the development of new manufacturing technologies.

1. SIMULATION OF THE STRUCTURAL EVOLUTION UNDER HOT PLASTIC DEFORMATION

1.1. Dynamic Strain Hardening and Recovery

The first significant structural changes caused by plastic deformation at both room and high temperatures are associated with the processes of dynamic work hardening and recovery (Fig. 2, stage I). This stage is well described by the models proposed by Kocks, Mecking, Estrin [14–16], and Nes [17–19]. These models describe the evolution of the dislocation structure by the following law:

$$\frac{d\rho}{d\varepsilon} = \frac{d\rho^+}{d\varepsilon} + \frac{d\rho^-}{d\varepsilon}, \quad (1)$$

where ρ is the dislocation density (m^{-2}) and ε is the strain degree.

The first term in Eq. (1) stands for the athermal formation of dislocation pileups, which for single-phase coarse-grained materials can be determined from the following equation [16]:

$$\frac{d\rho^+}{d\varepsilon} = \frac{2}{b_B L} = k_1 \sqrt{\rho}, \quad (2)$$

for multiphase materials and alloys with a micrograin structure:

$$\frac{d\rho^+}{d\varepsilon} = k, \quad (3)$$

where b_B is the abs. value of Burgers vector (m), L is the average distance covered by a dislocation to full stop (m), k_1 and k are constants, determining strain-induced hardening. The constants depend on the nature and concentration of alloying elements in a solid solution, the volume fraction of phases, and others. The value of constants is determined using experimental data. The second term describes dynamic recovery. The rate of recovery is usually determined by the first-order reaction equation (the question of why it is proportional to the first degree of forest dislocation number density is a subject of discussion [20], but this dependence is in agreement with experimental data):

$$\frac{d\rho^-}{d\varepsilon} = -k_2 \rho, \quad (4)$$

where k_2 is the constant that depends on many factors (temperature, concentration of alloying elements, energy of diffusion activation, stacking fault energy, and others). The coefficient k_2 is difficult to calculate.

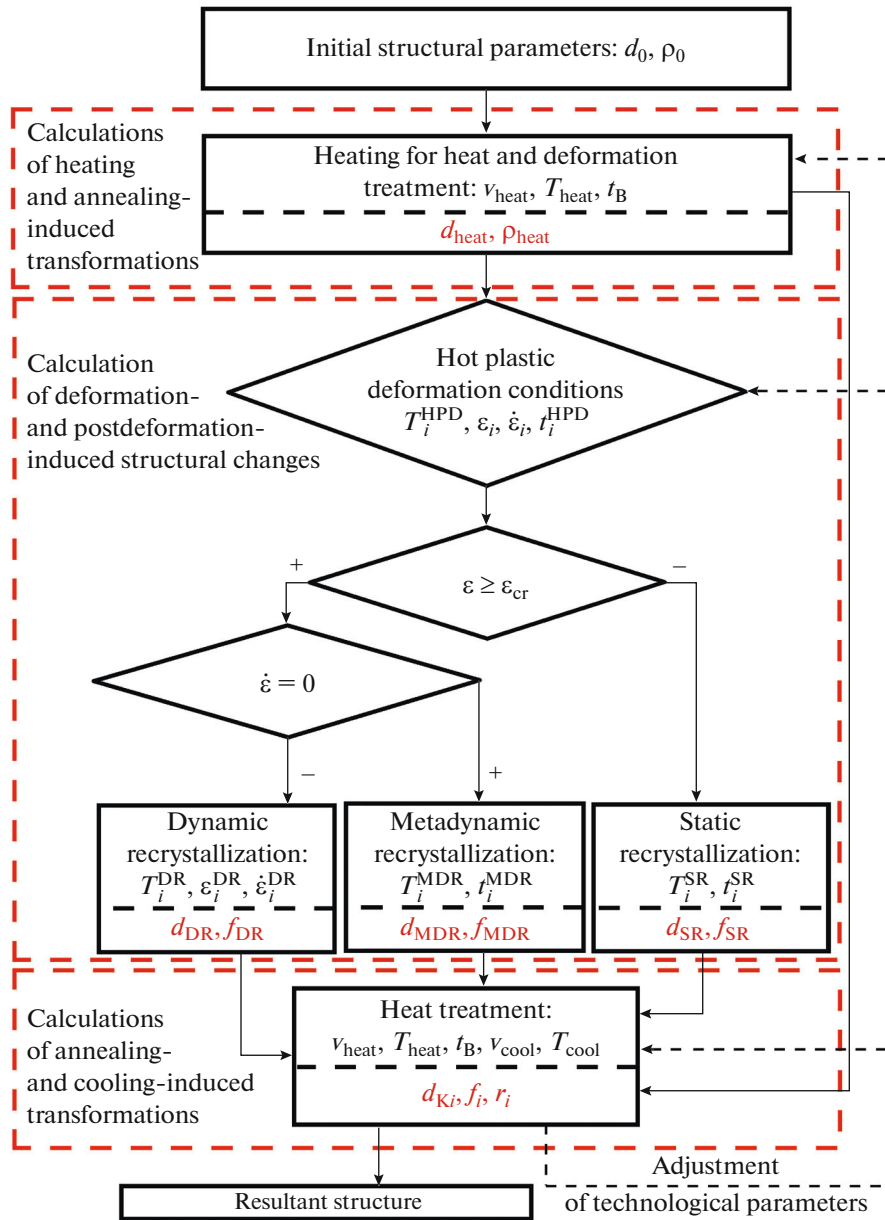


Fig. 1. Algorithm for calculating the structural formation process during heat and deformation treatment of metal materials.

It is determined on the basis of experimental data for some alloys. Authors [21] have shown that k_2 for armco iron varies in the range 5.8–42.5 depending on the temperature and strain rate. The power dependence of this constant on the Zener–Hollomon parameter $Z = \dot{\epsilon} \exp\left(\frac{602100}{RT}\right)$ was also found for titanium alloy TA15 [22]:

$$k_2 = 1.2 \times 10^7 Z^{-0.16}. \tag{5}$$

$\dot{\epsilon}$ is the strain rate (s^{-1}), T is the temperature (K), and R is the universal gas constant.

The evolution of the dislocation structure during dynamic recovery upon deformation at elevated temperatures in most cases initiates the formation of a subgrain microstructure. The steady-state stage in case of the suppression of dynamic recrystallization due to rapid dynamic recovery processes is characterized by the constant average size of subgrains, their constant dislocation angle, and the constant average density inside the subgrains. The average subgrain size (d_s) can be determined using the dislocation density calculated by Eq. (1), and provided that the disloca-

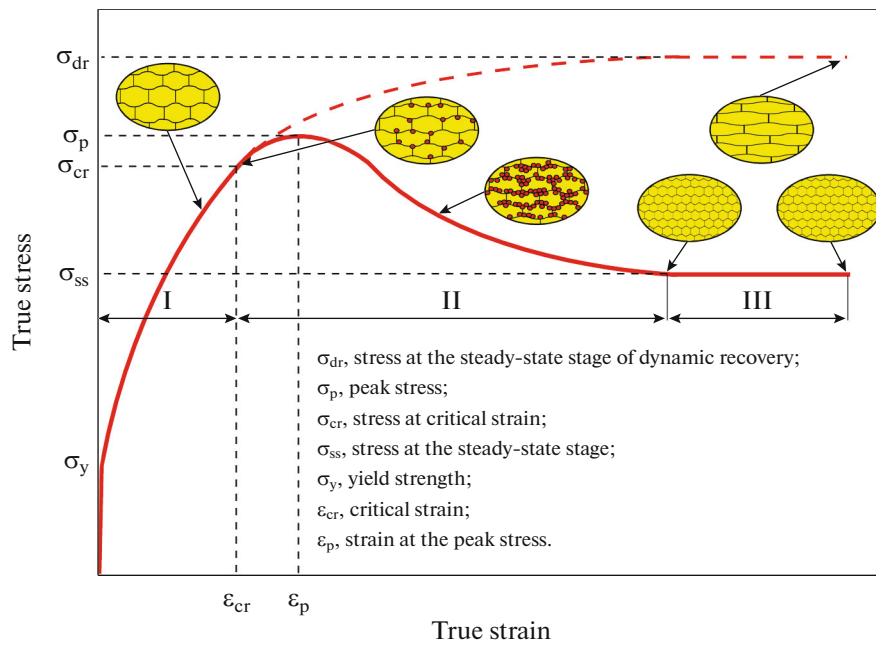


Fig. 2. Schematic structural changes and stress–strain dependence during hot plastic deformation of metallic materials [21]. (I) dynamic recovery, (II) dynamic recrystallization, and (III) steady-state flow.

tion density inside subgrains is much lower than the average dislocation density:

$$d_s = \frac{3\sin\varphi}{b_B\rho}, \quad (6)$$

where φ is the misorientation angle between subgrains. The misorientation angle between subgrains φ at the steady-state stage is usually 1.5° – 2° .

In practice, the identification of unknown coefficients k_1 and k_2 does not require rigorous structural research. Their values and rate and temperature dependencies can be found from the initial region of the strain curve, knowing the relationship between the yield strength and dislocation density [23]:

$$\sigma = \sigma_0 + \alpha G b_B \sqrt{\rho}, \quad (7)$$

where σ_0 is the yield strength that is not constrained by the resistance of newly generated dislocations (approximately corresponds to the yield strength), α is the constant coefficient ($\alpha \approx 1$), and G is the shear modulus (MPa). The parameters of a substructure can be determined with sufficient accuracy by the region of the strain curve from the beginning to the attainment of a critical strain degree.

1.2. Dynamic Recrystallization

After achieving a critical deformation, the softening due to dynamic recovery is accompanied by the nucleation of new grains with a perfect structure. These grains also undergo strain hardening, which

may lead to the formation of new grains within them. This process is called dynamic recrystallization.

The kinetics of phase and structural transformations is known to be well described by the Johnson–Mehl–Avrami–Kolmogorov model (JMAK) [24–26]:

$$X = 1 - \exp[-\beta t^n], \quad (8)$$

where X is the fraction of the transformed substance, t is the time (s), β and n are constants.

Equation (8) in the case of dynamic recrystallization can be put in the form:

$$X_{DRX} = 1 - \exp[-\beta((\varepsilon - \varepsilon_{cr})/(\varepsilon_{0.5} - \varepsilon_{cr}))^{k_d}], \quad (9)$$

where X_{DRX} is the volume fraction of dynamically recrystallized grains and ε_{cr} is the critical strain degree that empirically depends on the initial grain size (d_0) and the Ziner–Hollomon parameter:

$$\varepsilon_{cr} = a_1 d_0^n \dot{\varepsilon}^m \exp\left[\frac{Q_1}{RT}\right], \quad (10)$$

$\varepsilon_{0.5}$ is the strain degree at which 50% of recrystallized grains are formed in the structure. This value is usually determined by the degree of softening caused by dynamic recrystallization and corresponds approximately to the yield strength:

$$\sigma_{0.5} = \frac{\sigma_p - \sigma_{ss}}{2}. \quad (11)$$

where σ_p is the maximum yield strength (MPa) and σ_{ss} is the yield strength at the steady-state stage (MPa).

Table 1. Mathematical models of structural evolution during dynamic recrystallization

Material	Volume fraction of dynamically-recrystallized grains	Size of dynamically-recrystallized grains d_{DRX} , μm	Reference
EP666	$k_d = 1.76, \varepsilon_{\text{cr}} = 0.014\dot{\varepsilon}^{0.06} \exp\left[\frac{28930}{RT}\right],$ $\varepsilon_{0.5} = 0.053\dot{\varepsilon}^{0.05} \exp\left[\frac{27200}{RT}\right]$	$8826\dot{\varepsilon}^{-0.01} \exp\left(\frac{69800}{RT}\right)$	[39]
AISI 316	$k_d = 0.029\dot{\varepsilon}^{-0.04} \exp\left[-\frac{16550}{RT}\right],$ $\varepsilon_{\text{cr}} = 1.97\dot{\varepsilon}^{0.06} \exp\left[\frac{23590}{RT}\right],$ $\varepsilon_{0.5} = 71\dot{\varepsilon}^{0.124} \exp\left[\frac{51300}{RT}\right]$	$0.3\dot{\varepsilon}^{-0.123} \exp\left(\frac{50900}{RT}\right)$	[40]
AISI 310S	$k_d = 1.78, \varepsilon_{\text{cr}} = 0.0175\dot{\varepsilon}^{0.063} \exp\left[\frac{33390}{RT}\right],$ $\varepsilon_{0.5} = 0.05\dot{\varepsilon}^{0.056} \exp\left[\frac{28900}{RT}\right]$	$3062\dot{\varepsilon}^{-0.067} \exp\left(\frac{60970}{RT}\right)$	[41]
15Kh2NMFA	$k_d = 3.42, \varepsilon_{\text{cr}} = 0.022d_0^{0.029}\dot{\varepsilon}^{0.13} \exp\left[\frac{26900}{RT}\right],$ $\varepsilon_{0.5} = 0.022d_0^{0.076}\dot{\varepsilon}^{0.1} \exp\left[\frac{32600}{RT}\right]$	$314302d_0^{-0.01}\dot{\varepsilon}^{-0.1} \exp\left(\frac{111400}{RT}\right)$	[42]
30KhN3M2FA	$k_d = 3.74, \varepsilon_{\text{cr}} = 0.076d_0^{0.019}\dot{\varepsilon}^{0.048} \exp\left[\frac{10900}{RT}\right],$ $\varepsilon_{0.5} = 0.19\dot{\varepsilon}^{0.44} \exp\left[\frac{7900}{RT}\right]$	$63900d_0^{-0.01}\dot{\varepsilon}^{-0.09} \exp\left(\frac{96000}{RT}\right)$	[42]

It was shown empirically that the value of $\varepsilon_{0.5}$ also depends on the initial grain size and the Ziner–Hollomon parameter:

$$\varepsilon_{0.5} = a_2 d_0^{m_2} \dot{\varepsilon}^{m_2} \exp\left[\frac{Q_2}{RT}\right], \quad (12)$$

where $a_1, a_2, n_1, n_2, m_1, m_2, Q_1, Q_2$, and k_d are the parameters of a material, which can be found experimentally, $\beta = \ln(2) = 0.693$.

The size of dynamically-recrystallized grains at the steady-state stage practically does not depend on the strain degree and is determined only by the initial grain size, strain rate, and temperature:

$$d_{\text{DRX}} = a_3 d_0^{n_3} \dot{\varepsilon}^{m_3} \exp\left(\frac{Q_3}{RT}\right), \quad (13)$$

where a_3, n_3, m_3 , and Q_3 are the parameters of a material, which can be determined from microstructural studies. Table 1 lists the values of these constants for some materials.

There are also special models for calculating the grain size for different types of dynamic recrystallization (continuous, discontinuous, geometric). Thus, the dynamically-recrystallized grain size for the geometric dynamic recrystallization (the term is proposed

by McQueen et al. in [27, 28]) is described by the model of Pettersen et al. [29]. The model describes the change in the grain size during deformation by the following differential equation:

$$\frac{dd_{\text{DRX}}}{d\varepsilon} = \frac{dd_{\text{DRX}}^+}{d\varepsilon} + \frac{dd_{\text{DRX}}^-}{d\varepsilon}, \quad (14)$$

where $\frac{dd_{\text{DRX}}^+}{d\varepsilon}$ is the dynamic grain growth and $\frac{dd_{\text{DRX}}^-}{d\varepsilon}$ is the grain refinement by changing its geometric shape and forming high angular boundaries. The rate of grain growth with increasing deformation is inversely proportional to the Ziner–Hollomon parameter and the actual grain size:

$$\frac{dd_{\text{DRX}}^+}{d\varepsilon} = \frac{K_G}{Zd_{\text{DRX}}}, \quad (15)$$

where K_G is the constant. The grain refinement in turn is described by the following empirical model:

$$\frac{dd_{\text{DRX}}^-}{d\varepsilon} = \left[1 - \left(\frac{1}{4}\varepsilon + 1\right)e^{-2\varepsilon}\right] n A d_{\text{DRX}} \left(\frac{d_{\text{DRX}}}{d}\right)^{1/n}, \quad (16)$$

where n and A are constants.

In addition, the kinetics of dynamic recrystallization and the grain growth are significantly influenced by second-phase nanoparticles [30], which reduce coefficient β in Eq. (8) according to dependence:

$$\beta \sim (P_d - P_z)^3, \quad (17)$$

where P_d is the driving force of grain growth during recrystallization in the particle-free matrix phase and P_z is the force of particle resistance to grain boundary movement.

$$P_d = \frac{Gb_B^2}{2}(\rho_{\text{def}} - \rho_0) + \frac{4\gamma}{d_{\text{DRX}}}, \quad (18)$$

$$P_z = \frac{3\gamma f}{2r}, \quad (19)$$

where ρ_{def} , ρ_0 are the dislocation density in the grains after deformation and recrystallization, respectively, γ is the specific energy of grain boundaries, and r and f are the radius and the volume fraction of the second-phase particles, respectively.

Models describing grain structure formation in materials containing micron-sized second-phase particles have also been developed. The more general approach is to apply the Ziner–Smith model [31], which was developed in the works of Gladman [32], Nishizava [33], and others. The general form of the equation relating the grain size to the parameters of the second-phase particles is as follows:

$$d = A \frac{r}{f^n}, \quad (20)$$

where A and n are the constants characterizing a material. This model has shown good results when calculating the grain size for the microalloyed steel [34] and two-phase aluminum alloys [35].

There is a difficulty in the calculation of dynamic recrystallization process, which is to determine the critical strain degree. Based on the thermodynamics of irreversible processes, Poliak and Jonas have determined that the moment of nucleation beginning corresponds to the point of inflection in the curve of the strain-hardening coefficient ($\partial\sigma/\partial\varepsilon$) as a function of the yield strength (σ) [36]. Another method for determining the moment when dynamic recrystallization starts, which is based on the critical dislocation gradient, is proposed by Imran and Bambach [37].

This method takes into account the nonuniform distribution of dislocations near boundaries and in the grain body during deformation. The evolution of a dislocation structure is described separately for mobile and pinned dislocations. New grains begin to nucleate only when the critical dislocation gradient is reached. However, empirical dependence of the critical strain degree as a function of the peak strain is most often used in practical application [38]: $\varepsilon_{\text{cr}} = 5/6\varepsilon_n$.

1.3. Metadynamic Recrystallization

Metadynamic recrystallization (MDR) starts after the deformation process stops at critical degree ε_{cr} . In fact, MDR is the growth of grains (nuclei) formed as a result of dynamic recrystallization. Therefore, this process takes place without the incubation period, which is typical of static recrystallization in a deformed metal.

The kinetics of metadynamic recrystallization can also be described by the JMAK model [43–45]:

$$X_{\text{MRX}} = 1 - \exp\left[-\beta\left(\frac{t}{t_{0.5}}\right)^{k_m}\right], \quad (21)$$

where X_{MRX} is the fraction of recrystallized grains, which in general should take into account the presence of dynamically recrystallized grains, t is the annealing time, $t_{0.5}$ is the time, at which 50% metadynamically recrystallized grains form in the structure, and k_m is the empirically determined constant. The value $t_{0.5}$ is shown empirically to depend on the initial grain size, strain rate, and temperature, just like in the case of dynamic recrystallization:

$$t_{0.5} = a_4 d_0^{n_4} \dot{\varepsilon}^{m_4} \exp\left[\frac{Q_4}{RT}\right], \quad (22)$$

where a_4 , n_4 , m_4 , and Q_4 are the parameters of the material. In some cases, the effect of the strain degree is added to Eq. (22), but in most cases this factor is neglected. The change in the grain size during the MDR process is described by the power law:

$$d_{\text{MRX}} = a_5 d_0^{n_5} \dot{\varepsilon}^{m_5} \exp\left(\frac{Q_5}{RT}\right), \quad (23)$$

where a_5 , n_5 , m_5 , and Q_5 are the parameters of the material. The microstructure of a material significantly influences the constants. For example, the authors of [46] show that increasing the volume fraction of the δ phase in the structure of high-temperature nickel alloy from 0 to 16.7% significantly reduces the effective energy of activation Q_4 of metadynamic recrystallization from 356 to 104 kJ/mol. However, this model has a disadvantage. It cannot take the kinetics of grain size change during MDR into account. Obviously, recrystallization nuclei growth at the initial stage should be significant (for example, for 300M steel in Fig. 3 [45]), which does not allow applying Eq. (23) for calculation. Therefore, Eq. (23) should be changed to take into account grain growth at the initial stage of recrystallization, for example, by introducing an additional exponential multiplier:

$$d'_{\text{MRX}} = d_{\text{MRX}}^0 + (d_{\text{MRX}} - d_{\text{MRX}}^0)(1 - \exp(-k_{\text{MRX}}t)), \quad (24)$$

where d_{MRX}^0 is the initial grain size and k_{MRX} kinetic constant of grain growth. Figure 3 illustrates a model application.

However, the model (Eq. (23)) gives satisfactory results in most practical applications. The values of

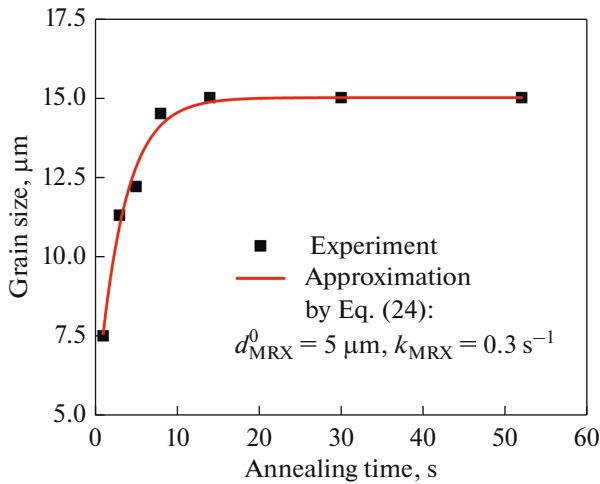


Fig. 3. Grain size as a function of the time of metadynamic recrystallization of steel 300 M after deformation at a rate of 0.01 s^{-1} at 1000°C [44].

constants determining the behavior of some materials upon MDR are presented in Table 2.

1.4. Static Recrystallization

If the critical strain during hot plastic deformation is not achieved but the accumulated internal energy is

enough to form new grain nuclei, static recrystallization (SR) takes place. Similar to metadynamic recrystallization, the main characteristics, determining the kinetics of the process, are power k_s and time $t_{0.5}$ at which 50% recrystallized grains form in the structure.

$$X_{\text{SRX}} = 1 - \exp\left[-\beta\left(\frac{t}{t_{0.5}}\right)^{k_s}\right]. \quad (25)$$

Despite the incubation period required for nucleation, the equations describing $t_{0.5}$ and k_s , are similar to those used to describe MDR. However, the accumulated deformation in the case of static recrystallization plays a significant role [50]:

$$t_{0.5} = a_6 d_0^{n_6} \dot{\epsilon}^{m_6} \epsilon^{h_6} \exp\left[\frac{Q_6}{RT}\right], \quad (26)$$

$$d_{\text{SRX}} = a_7 d_0^{n_7} \dot{\epsilon}^{m_7} \epsilon^{h_7} \exp\left(\frac{Q_7}{RT}\right), \quad (27)$$

where a_6 , a_7 , n_6 , n_7 , m_6 , m_7 , h_6 , h_7 , Q_6 , and Q_7 are the constants of a material. Table 3 lists the values of these constants for some materials.

A large number of structural studies are required to determine the unknown constants. The recrystallized grain size can be determined in situ using a laser microscope [53] and laser ultrasonic measurement [53–56]. To decrease the number of structural studies, special techniques are used to monitor the kinetics of recrystallization using the degree of softening after

Table 2. Mathematical models of kinetics and grain size changes during MDR

Material	Volume fraction of metadynamically-recrystallized grains	Size of metadynamically-recrystallized grains d_{MRX} , μm	Reference
SA508-III steel	$k_m = 0.508$, $t_{0.5} = 9.8 \times 10^{-5} \dot{\epsilon}^{-0.335} \exp\left[\frac{116\,210}{RT}\right]$	$\begin{cases} 472.8 \dot{\epsilon}^{-0.205} \exp\left(\frac{-23\,800}{RT}\right), \\ \text{if } d_0 \geq 120 \mu\text{m} \\ 12.5 \dot{\epsilon}^{-0.23} d_0^{0.758} \exp\left(\frac{-23\,800}{RT}\right), \\ \text{if } d_0 < 120 \mu\text{m} \end{cases}$	[47]
Steel Fe–C–Mn	$k_m = 1.5$, $t_{0.5} = 1.1 \dot{\epsilon}^{-0.8} \exp\left[\frac{-10\,000}{RT}\right]$	$26\,000 \dot{\epsilon}^{-0.23} \exp\left(\frac{-69\,000}{RT}\right)$	[43, 48]
Steel 300M	$k_m = 1.21$, $t_{0.5} = 0.049 \dot{\epsilon}^{0.039} \exp\left[\frac{-49\,770}{RT}\right]$	$62.36 \dot{\epsilon}^{0.076} \exp\left(\frac{-11\,535}{RT}\right)$	[45]
Steel 316	$k_m = 0.237$, $t_{0.5} = 2.14 \times 10^{-9} d_0 \dot{\epsilon}^{-0.85} \exp\left[\frac{155\,000}{RT}\right]$	$1.57 d_0^{0.99} \dot{\epsilon}^{-0.033} \exp\left(\frac{-5115}{RT}\right)$	[40]
Steel 30Cr2Ni4MoV	$k_m = 0.31$, $t_{0.5} = 1.27 \times 10^{-9} \dot{\epsilon}^{-0.44} \exp\left[\frac{217\,800}{RT}\right]$	$\begin{cases} 4059 \dot{\epsilon}^{-0.22} \exp\left(\frac{-47\,900}{RT}\right), \\ \text{if } d_0 \geq 225.4 \mu\text{m} \\ 0.28 \dot{\epsilon}^{-0.22} d_0^{1.77} \exp\left(\frac{-47\,900}{RT}\right), \\ \text{if } d_0 < 225.4 \mu\text{m} \end{cases}$	[49]

Table 3. Mathematical models of kinetics and grain size changes during static recrystallization

Material	Volume fraction of statically-recrystallized grains	Size of statically-recrystallized grains d_{SRX} , μm	Reference
Steel 300M	$k_s = 0.114, t_{0.5} = 5.4\dot{\epsilon}^{-0.181} \exp\left[\frac{32\,200}{RT}\right]$	$2378\dot{\epsilon}^{0.233} \exp\left(\frac{-53130}{R \cdot T}\right)$	[51]
Steel 316	$k_s = 0.31, t_{0.5} = 3.72 \times 10^{-8} \dot{\epsilon}^{-2.2} \dot{\epsilon}^{-0.66} \exp\left[\frac{137\,000}{RT}\right]$	$0.57d_0 (t_{0.5})^{0.042}$	[40]
Steel Ti–Nb–HSLA	$k_s = 0.6,$ $t_{0.5} = \begin{cases} 1.18 \times 10^{-11} \dot{\epsilon}^{-1.31} \dot{\epsilon}^{-1.07} d_0^{0.353} \exp\left(\frac{240\,000}{RT}\right), & \text{if } T < 1150^\circ\text{C} \\ 3.81 \times 10^{-4} \dot{\epsilon}^{-1.31} \dot{\epsilon}^{-1.07} d_0^{0.353} \exp\left(\frac{35\,400}{RT}\right), & \text{if } T \geq 1150^\circ\text{C} \end{cases}$	$8.49\dot{\epsilon}^{-0.872} d_0^{0.33} \exp\left(\frac{-10\,600}{RT}\right)$	[52]

Table 4. Constants in Eq. (28)

Material	n_s	k_{gg}	Q_8	Reference
Steel Ti–HSLA	10	2.6×10^{28}	437000	[59]
Steel Nb–HSLA	4.5	4.05×10^{23}	435000	[59]
Steel 12Kh2NMFA	4	8.4×10^{17}	357720	[42]
26KhN3MFA	4	6.4×10^{16}	347000	[42]

deformation. This technique involves an additive effect of deformed and recrystallized regions of a material on the yield strength. Moreover, there are two ways to determine the time when the half volume of the material is recrystallized during MDR and SR (Fig. 4) [57, 58]. The first way is to load and deform a material insignificantly (until the yield strength is reached) within certain time periods τ_1 , τ_2 , and τ_N to estimate the material response to this effect. The second way is to measure the stress relaxation curve continuously after deformation. The time required for the yield strength to decrease by half ($\sigma_{0.5}$) must correspond to the time required for material to recrystallize by half ($t_{0.5}$). Both methods have an essential drawback, because of recovery processes playing an essential role at the initial stage of relaxation. Their influence must be considered according to the method proposed by Karjalainen [57]. In addition, even a slight additional deformation under multiple loading can affect the accuracy of the determination of kinetic parameters.

1.5. Grain Growth during Annealing

The system tends to reduce internal energy, including by reducing the number of defects, which leads to

grain growth in metal materials at increased temperatures, regardless of the presence of internal defects. This process is also sometimes called collective recrystallization or normal grain growth. The main factors affecting the growth rate and, as a consequence, the final grain size, are the annealing time and temperature. The following dependence is generally accepted:

$$d^{n_8} = d_0^{n_8} + k_{gg} t \exp\left(\frac{-Q_8}{RT}\right), \quad (28)$$

where n_8 , Q_8 , k_{gg} are the constants of a material. Theoretically, constant n_8 is 2, but in most cases, its value is much higher due to a large number of factors affecting the pinning of grain boundaries (atoms dissolved at grain boundaries, phase precipitates, and others). Table 4 lists the values of the constants that determine grain growth during collective recrystallization for some materials.

Input parameters for calculating the structure in materials at the final stages of heat and deformation treatment can be calculated using the models describing structural evolution during hot plastic deformation.

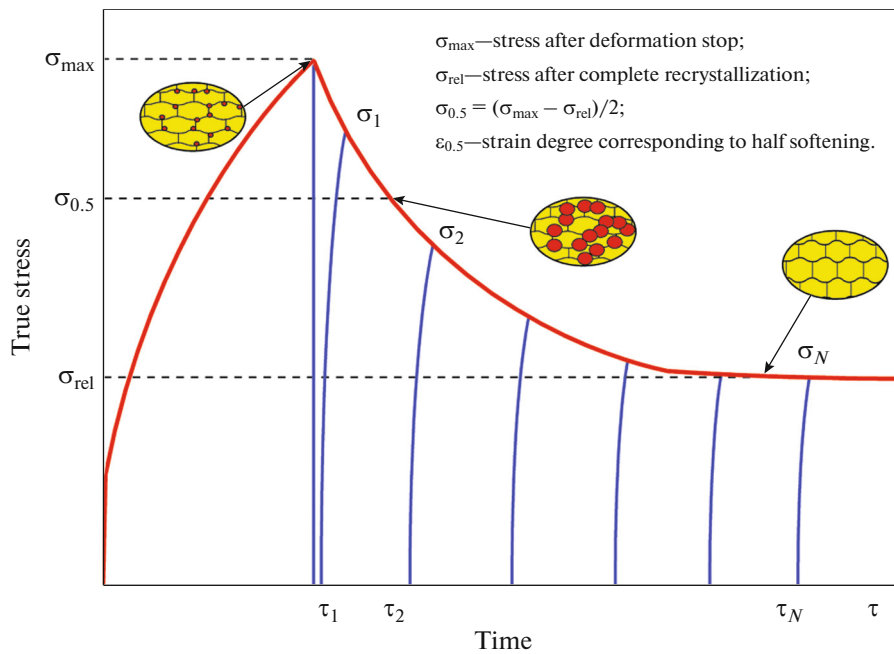


Fig. 4. Schematic for determining the kinetics of metadynamic and static recrystallization by multiple loading for determining the relaxation curve.

2. SIMULATION OF PHASE TRANSFORMATION KINETICS IN STEELS

2.1. Austenite Formation during Heating

Transformations in carbon and alloy steels during heating and cooling are crucial for structure and property formation. Heating of a ferritic–pearlitic mixture above the A_{c1} point results in austenite formation, where nuclei mainly form at the boundaries of ferritic grains and pearlitic colonies. The kinetics of austenite formation can be described by the classical theory of the formation and growth of nuclei. According to Liu et al. [60], the rate of nucleation in the case of overheating is described by the Arrhenius law:

$$N = N_0 \exp\left(-\frac{Q_N}{RT}\right), \quad (29)$$

where Q_N is the threshold energy of the atomic migration through the interface. The preexponential multiplier N_0 depends on a large number of factors, such as the heating rate, pearlitic colony size, and ferritic grain size. For example, the rate of austenite nucleation in the 22MnB5 steel microstructure can be [61]:

$$N = (A_0 + A_1 v^{m_A}) \exp\left(-\frac{Q_N}{RT}\right), \quad (30)$$

where A_0 , A_1 , m_A are the constants of a material, which can be found using experimental data, and v is the heating rate.

The rate of nucleus growth in the case of overheating is also mainly determined by diffusion and is described by the following equation:

$$v = v_0 \exp\left(-\frac{Q_v}{RT}\right), \quad (31)$$

where Q_v is the effective activation energy of the growth and v_0 is the preexponential factor. The rate of the growth of volume fraction (f) of the austenitic phase can be determined by combining Eqs. (30) and (31) as follows:

$$\frac{df}{dt} = v \int N dt. \quad (32)$$

where t is the time (s).

The model is simple, but a significant number of assumptions severely limit its use. First, the model must be artificially restricted to stop nucleation (for example, when the volume fraction of austenite exceeds the pearlitic volume fraction [61]). In addition, the model does not limit the threshold volume fraction and the attenuation of its growth. In this regard, the model must be converted to a form that takes into account a decrease in the reaction volume (JMAK model):

$$\frac{df^R}{dt} = (1 - f^R) \frac{df}{dt}, \quad (33)$$

where f^R is the factual volume fraction of austenite.

This model becomes much more complicated if we take into account the geometry of growing austenitic

grains and that austenization may not occur completely [62]. Considering the growth of grains to be radial, Eq. (32) can be changed to the following form:

$$\frac{df}{dt} = 4\pi R_\gamma^2 \frac{dR_\gamma}{dt} \int N dt, \quad (34)$$

where R_γ is the radius of an austenitic grain (assuming unlimited growth). The phase growth depends on the atomic mobility ($M^{\alpha\gamma}$) at the α/γ interface and the driving force of the $\alpha \rightarrow \gamma$ transformation ΔG^γ :

$$\frac{dR_\gamma}{dt} = M^{\alpha\gamma} \Delta G^\gamma. \quad (35)$$

$M^{\alpha\gamma}$ can be described by the Arrhenius equation:

$$M^{\alpha\gamma} = M_0^{\alpha\gamma} \exp\left(-\frac{Q_\gamma}{RT}\right), \quad (36)$$

where $M_0^{\alpha\gamma}$ and Q_γ are the preexponential factor and the effective activation energy of interphase movement, respectively.

The driving force of the transformation is proportional to the equilibrium volume fraction of austenite f_{eq}

$$\Delta G^\gamma = \Delta G_0^\gamma (f_{eq} - f), \quad (37)$$

where ΔG_0^γ are the coefficients of proportionality. Thus, the equation of kinetics of austenite formation has its final form:

$$\begin{aligned} \frac{df}{dt} = & (36\pi)^{\frac{1}{3}} N dt^{\frac{2}{3}} f^{\frac{2}{3}} M_0^{\alpha\gamma} \Delta G_0^\gamma \\ & \times \exp\left(-\frac{Q_\gamma}{RT}\right) (f_{eq} - f). \end{aligned} \quad (38)$$

The parameters of the model can be determined using dilatometric research. For example, models describing the austenization of a 55CrMo steel during isochronous heating and isothermal exposure were constructed in [63].

In addition, there are empirical models for determining the size of austenitic grain (d_γ) after heating and holding at a certain temperature [64]:

$$d_\gamma = A_\gamma t^{C_\gamma} \exp\left(-\frac{b_\gamma}{T}\right), \quad (39)$$

where A_γ , C_γ , and b_γ are the experimentally-determined constants.

Models simulating the formation of austenite during heating in combination with calculation of grain growth during collective recrystallization have a great practical application for describing the refinement of austenitic grains before final heat treatment.

2.2. Processes of Austenite Transformation during Cooling

The simulation of structure formation during austenite decomposition is an important stage in selecting the optimal process parameters for heat treatment of steel. The formation of ferrite, pearlite, and bainite by the diffusion mechanism during cooling of steel depends on the temperature and time of the process and is well described by the JMAK model (Eq. (8)). In this case, the Avrami index is ~ 1 for ferrite formation, ~ 2 for perlite, and ~ 4 for bainite [65]. For continuous cooling conditions, Kamamoto [66] suggested using dimensionless parameter τ instead of time in Eq. (8):

$$\tau = \frac{T_b - T}{T - T_c}, \quad (40)$$

where T_b , T_c are the temperatures of the beginning and end of the process.

The decomposition of austenite by the diffusion mechanism is also usually described by the model of the formation and growth of nuclei. This model was considered when modeling the kinetics of austenite formation upon heating. However, one should keep in mind that the decomposition process produces several types of its products. Johns and Bhadeshia proposed a model describing the possibility of simultaneous precipitation of ferrite and perlite during the decomposition of supercooled austenite [67]. In this case, the kinetics of the precipitation of both phases depends on their volume fraction:

$$\begin{aligned} f^\alpha = & \left(\frac{1}{1+K}\right) \\ & \times \left[1 - \exp\left(-\frac{1}{3}(1+K)\pi\left(\frac{dR_\alpha}{dt}\right)^3 N_\alpha t^4\right)\right], \end{aligned} \quad (41)$$

$$\begin{aligned} f^p = & \left(\frac{K}{1+K}\right) \\ & \times \left[1 - \exp\left(-\frac{1}{3}\left(\frac{1+K}{K}\right)\pi\left(\frac{dR_p}{dt}\right)^3 N_p t^4\right)\right], \end{aligned} \quad (42)$$

where N_α , N_p , $\frac{dR_\alpha}{dt}$, $\frac{dR_p}{dt}$ are the rates of the nucleation and growth of ferrite (α) and pearlitic (p) colonies and K is the relation between the volume fractions of pearlite and ferrite. Its value can be determined as:

$$K = \frac{\left(\frac{dR_p}{dt}\right)^3 N_p}{\left(\frac{dR_\alpha}{dt}\right)^3 N_\alpha}. \quad (43)$$

Isothermal transformation diagrams (TTT diagrams) and continuous cooling transformation diagrams (CCT diagrams) are usually used for analysis of phase transformations during cooling of austenite. Their calculation would make it possible to predict

the microstructure in steel after different cooling treatments. In general, the TTT-diagrams can be described by the equation proposed by Zener [68] and Hillert [69]:

$$t(f, T) = \frac{F(Comp, d)}{\Delta T^n \exp\left(-\frac{Q}{RT}\right)} S(f), \quad (44)$$

where $F(Comp, d)$ is the function that depends on the steel composition and the austenitic grain size, ΔT is the supercooling degree relative to the start of the transformation, Q is the effective energy of transformation activation, n is the constant specifying the diffusion mechanism, and $S(f)$ is the function describing the transformation rate [70]:

$$S(f) = \int_0^f \frac{df}{f^{0.4(1-f)} (1-f)^{0.4f}}. \quad (45)$$

The martensite transformation is mainly determined by its temperature only. Koistinen and Marburger proposed the following type of model to describe a diffusionless transformation [71]:

$$X(T) = 1 - \exp[-\beta_m (M_s - T)], \quad (46)$$

where β_m is the constant (for example, for carbon steels its value is 1.1×10^{-2}), M_s is the temperature of the start of martensite transformation. Lee et al. modified this model by adding a multiplier that takes into account the presence of the transformed phase, which limits the further movement of the transformation front [72]:

$$\frac{df_m}{dT} = \alpha (M_s - T)^n f_m^{\varphi_m} (1 - f_m)^{\psi_m}, \quad (47)$$

where α , n , φ_m , ψ_m are the parameters of a material.

The models considered have been successfully applied in calculation of phase transformations in BR1500HS [73], HC380WD [6], 22MnB5 [74], and 1045 [75] steel during cooling of austenite. In addition, they are widely used to calculate the hardening of steel parts during cooling using software tools (such as Deform and Abaqus software programs) based on the finite element method [76, 77].

3. SIMULATION OF THE STRUCTURAL EVOLUTION UNDER SUPERSATURATED SOLID SOLUTION DECOMPOSITION

The decomposition of a supersaturated solid solution is one of the final stages of structure and property formation in precipitation-hardening alloys. To achieve the maximum strength properties, nanoscale particles should be uniformly distributed over the entire volume of the material. To this end, it is useful to simulate the structure beforehand to select the best heat treatment conditions. Starink et al. [78] proposed

a model of particle nucleation and growth during annealing, which is similar to the Johnson–Mehl–Avrami–Kolmogorov model. According to this model, the cluster with volume V_p grows in accordance with the equation:

$$V_p = A_p [G(t - \zeta)]^{m_p}, \quad (48)$$

where G is the average growth rate, A_p , m_p are the constants, and ζ is the time taken by a particle to form. The Kampmann–Wagner model predicts structural transformations during heating, such as the nucleation, growth, and enlargement of particles [79, 80]. The model is usually applicable to spherical-shaped particles [81, 82]. However, in some cases, for example, in 6xxx alloys, the model was tested on needle-shaped precipitates [83].

The authors of [84] adapted the Zener–Hillert equation to calculate the growth rate of needle-shaped precipitates of the metastable β -phase modification:

$$\frac{dl}{dt} = 1.5 \frac{D_{Mg}}{2r_p} \frac{X_{Mg} - X_{Mg}^i}{\alpha X_{Mg}^p - X_{Mg}^i} = 1.5 \frac{D_{Si}}{2r_p} \frac{X_{Si} - X_{Si}^i}{\alpha X_{Si}^p - X_{Si}^i}, \quad (49)$$

where X_{Mg} and X_{Si} are the solubility in Mg and Si matrices, respectively, X_{Mg}^i and X_{Si}^i their equilibrium solubility, X_{Mg}^p and X_{Si}^p are their solubility in particles, r_p is the particle radius, and α is the relation between the atomic volume of a matrix and a particle one. The model contains several significant assumptions:

(i) Particle nucleation is homogeneous. The elastic energy associated with particle formation is not taken into account. Therefore, the nucleation rate obeys the following law:

$$\frac{dN}{dt} = N_0 Z \beta^* \exp\left(\frac{G^*}{k_B T}\right) \left(1 - \exp\left(-\frac{t}{\tau}\right)\right), \quad (50)$$

where N_0 is the number density of nuclei, β^* is the rate of nucleus growth, Z is the Zel'dovich factor, and G^* is the activation energy of nucleation.

(ii) The particle shape factor remains constant regardless of the absolute particle size and is 11.

The model was adjusted in terms of structural parameters. It showed high accuracy in calculation of both β -phase particle parameters and the yield strength of an aluminum alloy 6061.

The models describing particle formation and growth showed also good accuracy in calculation of dispersoid formation in the aluminum alloy structure. Robson and Prangnell [85] proposed a model describing the kinetics of the precipitation and distribution of metastable $L1_2$ Al_3Zr -phase particles, depending on the zirconium concentration and homogenization annealing conditions. The model is also based on the Kampmann–Wagner model and takes into account

intracrystalline zirconium segregation during solidification. It also contains the following assumptions:

(i) Metastable precipitates have an exact stoichiometry of the Al_3Zr phase and are the only zirconium-enriched phase. Therefore, the model is applicable for 7xxx alloys.

(ii) The precipitates are distributed uniformly and the rate of their nucleation depends on the local zirconium concentration. Heterogeneous nucleation, which is possible only at grain boundaries, is excluded.

(iii) The particle growth is controlled by the diffusion of zirconium at the matrix/particle interface.

(iv) Zirconium atoms are distributed uniformly between the growing particles in the diffusion overlapping zones.

The nucleation rate of particles is described by the following classical Eq. [86]:

$$J = N_0 \frac{kT}{h} \exp\left(-\frac{G^* + Q}{kT}\right), \quad (51)$$

where J is the nucleation rate per volume unit, N_0 is the density of precipitations (number of zirconium atoms per volume unit in the case of homogeneous nucleation), and Q is the activation energy of zirconium diffusion in aluminum. Parameter G^* is calculated by the equation

$$G^* = \frac{4}{3} \pi r^{*2} \sigma. \quad (52)$$

The critical nucleus size is calculated according to the Gibbs–Thomson equation for solid solutions. The concentration at the boundary is equal to the average concentration in the matrix. There is no gradient at the grain boundary. r^* can be calculated from:

$$r^* = \frac{2\sigma V_a}{kT \ln \frac{c}{c_\infty^\alpha}}, \quad (53)$$

where V_a is atomic volume, c is the instant zirconium concentration in the matrix, and c_∞^α is the zirconium concentration in the matrix in the equilibrium with the Al_3Zr phase. The values of c_∞^α were obtained for the metastable Al_3Zr phase in the binary Al–Zr system by calculating the solvus from Saunders' work [87].

The equation of growth of spherical $L1_2$ -phase particles looks as follows:

$$\frac{dr}{dt} = \frac{D}{r} \frac{c - c_r^\alpha}{c^{a'} - c_r^\alpha}, \quad (54)$$

where D is the coefficient of diffusion, r is the particle radius, c_r^α is the zirconium concentration at the matrix/particle interface, and $c^{a'}$ is the zirconium concentration in a particle. c_r^α is calculated using c_∞^α

and the Gibbs–Thomson equation, which can be presented in general terms as:

$$c_r^\alpha = c_\infty^\alpha \exp\left(\frac{2\sigma V_a}{kT r}\right), \quad (55)$$

The segregation of zirconium can strongly affect the uniformity of particle distribution in a matrix. The effect of the composition and heat treatment conditions on the width of precipitation-free zones is particularly interesting.

The Scheil equation shows that the zirconium concentration in a solid phase (c_s) depends on the volume fraction of solid phases (f_s) during solidification [88].

$$c_s = k\bar{c} (1 - f_s)^{(k-1)}, \quad (56)$$

where \bar{c} is the average concentration of zirconium and k is the coefficient of proportionality. The change in the average particle size and its volume fraction can be calculated as a function of the distance from the periphery to the center of a dendritic cell.

A similar model is proposed for homogeneous and heterogeneous nucleation and growth of Al_3Sc particles [89]. These two models are combined in [90] for the simulation of hardening of a high-strength aluminum alloy alloyed with scandium and zirconium.

Clouet et al. propose another approach, which is based on cluster dynamics, to simulate the kinetics of Al_3Zr and Al_3Sc dispersoid formation [91]. This approach describes different stages of homogeneous nucleation and growth of dispersoids using only diffusion coefficients and the free energy of interphase boundaries. The rate of precipitate nucleation is described in this model by the following system of equations:

$$\beta_{n_x} = 4\pi \frac{D_X}{\Omega} r_{n_x} C_1 \frac{1 + kr^{\text{ext}}}{1 + k(r^{\text{ext}} - r_{n_x})}, \quad r_{n_x} \leq r^{\text{ext}}, \quad (57)$$

$$\beta_{n_x} = 4\pi \frac{D_X}{\Omega} r_{n_x} C_1 (1 + kr_{n_x}), \quad r_{n_x} \geq r^{\text{ext}}, \quad (58)$$

where D_X is the coefficient of diffusion of an element into a matrix, Ω is the atomic volume, r_{n_x} is the cluster radius, and r^{ext} is the half the interparticle distance.

In summary, high-precision models have been developed to calculate the volume fraction and the average size of the products of supersaturated solid solution decomposition. This, in turn, can predict the strength of aluminum alloys with high accuracy [92, 93].

4. COMPUTATIONAL METHODS FOR CALCULATING STRUCTURAL EVOLUTION

The development of computational techniques has resulted in a significant number of numerical methods

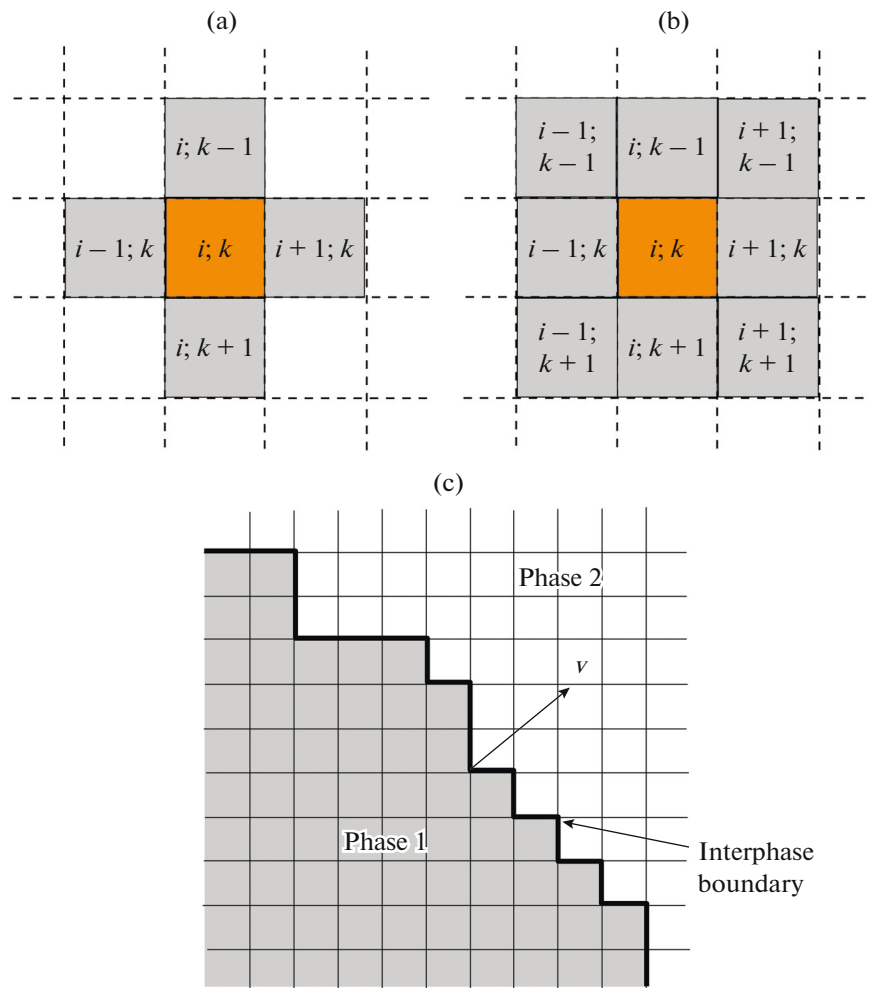


Fig. 5. Schematic position of neighbors of the cell described by (a) Neumann and (b) Moore. Schematic of interphase (grain) boundary motion in the calculation by the cellular automaton method [108].

for calculating the microstructure. The most common of these are the cellular automaton [94–98], the Monte Carlo [99–103], and the multiphase-field methods [104, 105]. In addition to calculating the quantitative microstructural characteristics, as the physical and mathematical models presented above do, these methods also provide information on the most probable distribution of certain microstructural elements in terms of phase and size due to the large number of analyzed elements.

4.1. Cellular Automaton Method

The main principle of the cellular automaton method is space and time discretization. Physical values, such as defect number density, structural-phase state characteristics, and others, take a set of values in each cell as a separate element of the microstructure. The state of the cells and the relationship between them at each moment of time is described by physical and probability relations. The state of each cell, that

is, a set of quantitative values characterizing the structural-phase state, is determined by external conditions and the previous state of a cell and its neighbors. Figures 5a and 5b exemplify the location of neighboring cells. The states of not only the immediate neighbors but also the neighbors from the second, third, and further rows may be taken into account. These values are updated simultaneously during the simulation in accordance with a set of preliminary specified transformation rules. This changes the state of the system as a whole, e.g., a shift of the interphase boundary (Fig. 5c). The cellular automaton method describes microstructural evolution in time and space terms. For example, the state of each element in the case of simulating the microstructural evolution during hot deformation can be determined by the following parameters: dislocation number density, crystallographic orientation, identification of belonging to a certain grain, and others. In addition, interaction between some network elements that determine the

kinetics of grain nucleation and growth should be described [106].

The general algorithm for constructing the microstructural evolution by the cellular automaton method includes the following stages.

(1) The volume being simulated is divided into N elements called cells.

(2) The initial state parameters are assigned to each cell and its neighbors.

(3) The new state of a cell at the next time step is calculated based on the states of its neighbors.

(4) The new state of the system is detected by iterating the states of all cells in the volume simulated. Thus the transition to the next step in time takes place.

The simple algorithm enables one to perform calculations using this method together with the finite element one. Thus, its functionality is considerably extended, allowing both static and dynamic structuring processes to be simulated. The main problem of the method is to find physical and probability laws of interaction between cells.

A static recrystallization model for a low-carbon 0.14C–0.2Si–0.4Mn steel was developed in [107]. The rate of nucleation N was described by the following equation:

$$N = M_N \exp\left(-\frac{Q_a}{RT}\right), \quad (59)$$

where Q_a is the activation energy of nucleation. Coefficient M_N can be found by the equation:

$$M_N = C_0 (H_i - H^c), \quad (60)$$

where C_0 is the constant, H_i is the amount of the stored energy in a cell, H^c is the critical energy required for nucleation, which depends on the critical strain degree (ε_c) and energy of low-angle boundaries γ_{lab} , the value of which is ~ 0.2 J/m²:

$$H^c = \frac{\varepsilon_c}{a\varepsilon_c + b} \gamma_{lab}, \quad (61)$$

where a and b are the experimentally-determined constants, whose values for aluminum alloys are 0.1×10^{-8} and 0.9×10^{-7} m, respectively [109]. The probability of nucleation in a certain cell was calculated as follows

$$P = NS_N t_{step}, \quad (62)$$

where S_N is the volume, where a nucleus can form and t_{step} is the time step.

The approach for calculation of the probability of nucleation is universal, but a simpler probabilistic approach is possible. According to it, the nucleation rate does not depend on the stored energy and the nucleation occurs at grain boundaries in a random way, proportionally to the area of nucleus-free boundaries. This approach was applied to calculate the static

recrystallization in a high-temperature nickel alloy [110].

The rate of recrystallization nucleus growth can be described as

$$V = Mp, \quad (63)$$

where p is the driving force of recrystallization and M is the grain boundary mobility, which is associated with the atomic diffusion mobility at a grain boundary.

$$M = \frac{Db_B^2}{kT}, \quad (64)$$

where D is the coefficient of grain boundary diffusion, b_B is the Burgers vector, and k is the Boltzmann constant.

The driving force depends on two factors: the difference between the dislocation number density ($\Delta\rho$ in the nucleus and a noncrystallized matrix):

$$P_\rho = 0.5Gb_B^2\Delta\rho, \quad (65)$$

where G is the tangential (shear) modulus of elasticity, and grain boundary energy dependent on the curvature of the boundary (κ):

$$P_g = \kappa\gamma_{hagb}, \quad (66)$$

where γ_{hagb} is the energy of a high-angle boundary (~ 0.6 J/m²):

$$\gamma_{hagb} = \begin{cases} \gamma_{hagb}^0, & \theta \geq \theta_0 \\ \gamma_{hagb}^0 \frac{\theta}{\theta_0} \left(1 - \ln\left(\frac{\theta}{\theta_0}\right)\right), & \theta < \theta_0 \end{cases}, \quad (67)$$

where γ_{hagb}^0 is the energy of a high-angle boundary with a critical misorientation angle $\theta_0 \approx 15^\circ$:

$$\gamma_{hagb}^0 = \frac{Gb_B\theta_0}{4\pi(1-\nu)}, \quad (68)$$

Where ν is the Poisson ratio. The curvature can be determined directly by analyzing the location of two or more layers closest to the analyzed cell [106]:

$$\kappa = \frac{A}{C_s} \frac{K - N_i}{N + 1}, \quad (69)$$

where A is the topological parameter ($A = 1.28$), C_s is the cell size, K is the number of cells, which form a flat boundary in the volume analyzed (i.e., in case of two layers of the nearest neighbors $K = 15$, in case of three $K = 28$), N_i is the number of cells that belong to the same grain as the analyzed cell, N is the total number of analyzed neighbors.

There is a good agreement between the data calculated by the JMAK model [107] and experimental results [111]. High-accuracy prediction of structural evolution during static recrystallization in the temperature range 970–1040°C after hot plastic deformation was demonstrated for high-temperature nickel

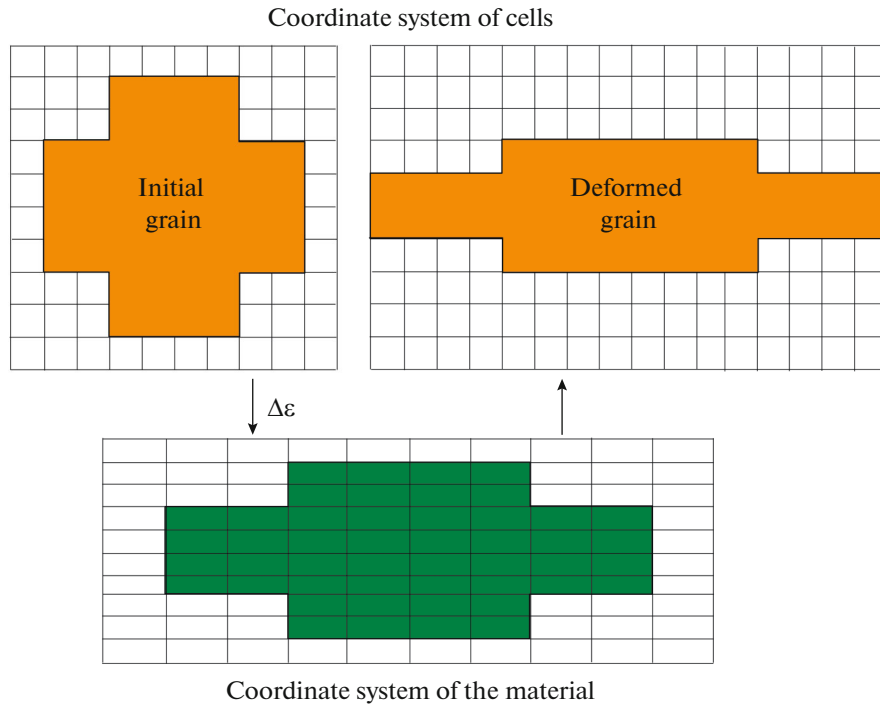


Fig. 6. Schematic transition from the coordinate system of a material to the coordinate system of cells after deformation [116].

alloy [110, 112] and cold-worked ferritic–pearlitic low-alloy steel [113].

The considered algorithm in the case of dynamic recrystallization is supplemented with a preliminary step to determine the possibility for the formation of a recrystallization nucleus, i.e. to achieve a critical dislocation density (in general, the total density of dislocations within boundaries and inside subgrains) in separate cells. The dislocation density as a function of hot plastic deformation conditions is described by the Kocks–Mecking–Estrin model (Eqs. (1)–(4)). The critical strain degree can be determined by the model of Poliak and Jonas [36]. The evolution of dislocation density in an integrated form at the dynamic recovery stage is described by the following formula:

$$\rho = \left[\frac{k_1}{k_2} - \frac{k_1}{k_2} \exp\left(-\frac{k_1}{k_2} \varepsilon\right) + \sqrt{\rho_0} \exp\left(-\frac{k_1}{2} \varepsilon\right) \right], \quad (70)$$

where k_1 and k_2 can be found using strain curves. These constants are related to each other as:

$$k_1 = \frac{\sigma_H k_2}{\alpha G b_B}, \quad (71)$$

where σ_H is the stress at the steady-state dynamic recovery stage (see Fig. 2) and α is the coefficient, the value of which is close to one.

In addition, for the process of dynamic recrystallization to be taken into account, into the equation for

calculating the rate of nuclei formation (59) the effect of strain rate is introduced [114]:

$$N = C_1 \dot{\varepsilon}^m \exp\left(-\frac{Q_a}{RT}\right), \quad (72)$$

where C_1 and m are the constants. The nucleation occurs only at grain boundaries, which is typical of discontinuous recrystallization. The orientation of the nuclei is specified arbitrarily.

The main difficulty in simulating the dynamic recrystallization process is a change in the grain shape, which affects the nucleation and nucleus growth. Therefore, the procedure of transition from the coordinates of the material to the coordinates of cells after each iteration is needed. The schematic transition is shown in Fig. 6. Grain boundary position during deformation changes in accordance with the following law as a result of this transformation [115]:

$$\begin{pmatrix} \mathbf{v}_1 \\ \mathbf{v}_2 \\ \mathbf{v}_3 \end{pmatrix} = \begin{pmatrix} e_{11} & e_{12} & e_{13} \\ e_{21} & e_{22} & e_{23} \\ e_{31} & e_{32} & e_{33} \end{pmatrix} \begin{pmatrix} \mathbf{u}_1 \\ \mathbf{u}_2 \\ \mathbf{u}_3 \end{pmatrix}, \quad (73)$$

where \mathbf{v}_i and \mathbf{u}_i are new and old vectors, determining the cell coordinates and e_{ik} is the strain matrix. However, this approach does not take into account the differences in the degree of deformation of old uncrystallized grains and new ones that grew from nuclei. The lower dislocation density enables new recrystallized grains to deform much more and, as a result, creates conditions for new nucleation. In addition, the scale

factor is also limiting, since the minimum grain size is the size of the cell simulated. To solve these problems, the authors [98] proposed the dimensional cell automaton method, which describes the dislocation distribution near the moving grain boundaries with high accuracy, and dynamically determines the minimum cell size required for the correct results.

Regardless of a considerable simplification and assumptions, this method showed high accuracy in calculation and good predicting ability when modeling dynamic recrystallization in a wide range of metallic materials. For example, Chen et al. [116] showed that the initial grain size influenced grain refinement in the austenitic stainless 316LN steel during hot plastic deformation. At an initial grain size of 450 μm , the volume fraction of recrystallized grains was only 43% even at a true strain of 3 ($\dot{\epsilon} = 1 \text{ s}^{-1}$, $t = 950^\circ\text{C}$). Liu et al. [117] simulated the grain refinement in the high-temperature nickel alloy during deformation. He showed a good correspondence between the calculated and experimental values of the grain size. He also determined the fact that dynamic recrystallization at the initial stage of deformation proceeds heterogeneously and becomes uniform only after reaching a certain degree of strain. Chen et al. [13] improved the calculation accuracy of the dynamic recrystallization process in 42CrMo steel by introducing the nucleation rate N (72) and grain boundary mobility (64) as power functions of the initial grain size. The kinetics of dynamic recrystallization in tool steel Cr₁₂MoV [118], medium-carbon steel 36Cr₂Ni₂Mo [119], pure copper [120], and magnesium alloy AZ80 [121] were described using the cellular automaton method and the JMAK model.

In addition to dynamic recrystallization, the cellular automaton method is used for the simulation of other thermomechanical processes. Yazdipour and Hodgson calculated the softening of austenitic stainless 304 steel after hot plastic deformation, which occurred due to static and metadynamic recrystallization [122]. The input parameters were the energy stored as a result of deformation, the volume fraction and the size of dynamically-recrystallized grains, the temperature, strain degree, and strain rate. The authors showed a significant deceleration of the softening process during dynamic recrystallization, which decreased the half-softening time with increasing degree, rate, and temperature of deformation.

The finite element method is also applicable for describing phase transformations. A good agreement between the calculation and the experiment was demonstrated by simulating the austenite decomposition in low-alloy steel [123], including that after deformation [124]. The authors found the kinetics of ferrite formation and its average grain size at cooling rates in the range 1–58°C/s, using thermodynamic data on carbon distribution between ferrite and austenite in the equation to determine the mobility of ferrite grain

boundaries. However, the calculation showed an equiaxed grain shape, whereas the true grain shape was elongated [125]. Yang et al. [126] simulated the austenization in steel 1070 at heating rates of 0.5–5°C/s, and suggested a method to eliminate the artificial anisotropy of grains that arises in the calculation. A significant influence of the annealing temperature and grain size on the chromium-containing carbide precipitation during the annealing of austenitic AISI 304 and 316 steels was shown by the cellular automaton method [127]. In addition, this method allows the calculation of the volume fraction, shape, and size of the bainite and martensite phases depending on the cooling rate of recrystallized or deformed austenite [95].

Monte Carlo Method

Similar to the cellular automaton method, the Monte Carlo method involves breaking a structure into separate elements forming a network. These elements are specified in the initial configuration according to the problem to be solved. The main principle of the Monte Carlo method is to minimize the total energy of the system by searching the local states of separate elements. The total energy of the system is described by Hamiltonian [128]:

$$E = \frac{J}{2} \sum_{i=1}^N \sum_{j=1}^m (1 - \delta_{S_i S_j}) + \sum_{i=1}^N H_{S_i}, \quad (74)$$

where J is the constant that scales grain boundary (interphase) energy, S_i , S_j are the numbers that determine orientation (belonging to a certain phase) of the current element and its neighboring cell (Fig. 7), and $\delta_{S_i S_j}$ is the Kronecker coefficient:

$$\delta_{S_i S_j} = \begin{cases} 1, & \text{if } S_i = S_j \\ 0, & \text{if } S_i \neq S_j \end{cases}, \quad (75)$$

N is the total number of elements in the system, m is the number of neighboring elements, and H_{S_i} is the internal energy of each element. When simulating the recrystallization process, the internal energy is primarily related to the dislocation density and is determined by the formula [129]:

$$H_{S_i} = \alpha G b_B^2 \rho_{S_i}. \quad (76)$$

First of all, the energy of the system is calculated for the initial state. After that, the state of one of the elements is changed to the state of its neighbor and the corresponding energy of the system is calculated. The difference in energy is used to identify the probable change in the state of the chosen element:

$$P = \begin{cases} 1, & \text{if } \Delta E \leq 0 \\ \exp\left(-\frac{\Delta E}{kT}\right), & \text{if } \Delta E > 0 \end{cases}. \quad (77)$$

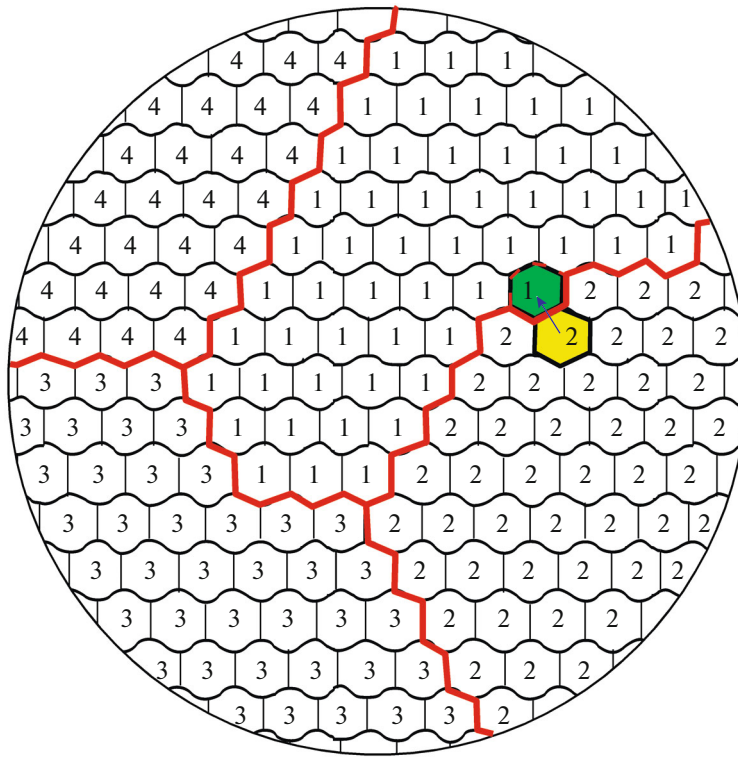


Fig. 7. Schematic orientation distribution of hexagonal elements by Monte Carlo method.

If the transition is possible, i.e. P is at least a random number from 0 to 1, the element changes its orientation (Fig. 7).

Even though the Monte Carlo method is a probability-based one, it gives good results for the structural simulation in most of the published works. This is explained by the fact that the initial stage and the kinetics of transformations depend on the energy of the system, which is governed by the structural parameters (e.g., dislocation density). The parameters can be found if we know some physical laws, such as the Kocks–Mecking–Estrin equation (1)–(4). The authors [128] have shown that the microstructure parameters for hot rolling of molybdenum-containing steel, which were calculated using this method, are comparable with the results simulated by the JMAK equation and are comparable with experimental data. The simulation of the static recrystallization process for this steel [99] showed that the change in the number of elements in the network from 40000 to 160000 does not affect the values of the calculated structural parameters significantly, changing only the visual representation of the calculation results. There is a good correlation with the experimental data in both cases. The Monte Carlo method was used to calculate the parameters of the texture formed during static recrystallization in α uranium [100], and also to predict the kinetics of copper particle precipitation in α iron during

annealing in the temperature range 250–500°C [101]. However, the main drawback of this method is the absence, in contrast to the cellular automaton method, of physical limitations to the movement of grain boundaries. This can lead to a dendritic shape of recrystallized grains, which is unusual for real processes [107].

4.3. Multiphase-Field Method

One more discrete method simulating the structural formation is the multiphase-field one. However, unlike the two approaches considered earlier, space and time discretization is made not at the stage when initial states are specified, but at the stage of solving differential equations describing the process of the structural evolution. The system state is described by the superposition of phase fields ϕ_i , that correspond to individual structural elements [130]. In the case of a polycrystal containing N grains, phase field ϕ_i , corresponds to each i th grain. The value of the field is 1 inside grain i , 0 outside grain boundaries, and $0 < \phi_i < 1$ at grain boundaries (Fig. 8).

Function ϕ_i is not independent and is limited to the following expression:

$$\sum_{i=1}^N \phi_i = 1. \quad (78)$$

The general state of the system is described by the following functional:

$$F = \int \left[\sum_{i=1}^N \sum_{j=i+1}^N \left(-\frac{a_{ij}^2}{2} \nabla \phi_i \cdot \nabla \phi_j + W_{ij} \phi_i \phi_j \right) + f_e \right] dV, \quad (79)$$

where a_{ij} is the energy gradient at grain boundaries:

$$a_{ij} = \frac{2}{\pi} \sqrt{2\delta\gamma_{ij}}, \quad (80)$$

where δ, γ_{ij} are the width and the energy of grain boundaries, respectively.

W_{ij} is the energy barrier height

$$W_{ij} = \frac{4\gamma_{ij}}{\delta}, \quad (81)$$

f_e is the density of the free energy inside grains.

The number of grains N in Eq. (79) can be replaced by $n = \sum_i^N \sigma_i$, where $\sigma_i = 1$, if $0 < \phi_i \leq 1$ and $\sigma_i = 0$ otherwise.

The phase field as a function of time looks like [131]

$$\frac{\partial \phi_i}{\partial t} = \sum_{j=1}^n \frac{2M_{ij}^\phi}{n} \left(\frac{\partial F}{\partial \phi_i} - \frac{\partial F}{\partial \phi_j} \right), \quad (82)$$

where M_{ij}^ϕ is the rate of phase boundary change, which depends on the grain boundary mobility (M_{ij}), is determined by the following expression:

$$M_{ij}^\phi = \frac{\pi^2 M_{ij}}{8\delta}. \quad (83)$$

Derivative of functional (79) for individual phase field functions takes the form:

$$\frac{\partial F}{\partial \phi_i} = \sum_{k=1}^n \left(W_{ij} \phi_k + \frac{a_{ij}^2}{2} \nabla^2 \phi_k \right) + \frac{\partial f_e}{\partial \phi_i}. \quad (84)$$

Taking into account that a difference is the driving force, we obtain:

$$\frac{\partial f_e}{\partial \phi_i} - \frac{\partial f_e}{\partial \phi_j} = -\frac{8}{\pi} \sqrt{\phi_i \phi_j} \Delta E_{ij}, \quad (85)$$

where ΔE_{ij} is the difference of accumulated energy in i th and j th grains, determined, for example, from Eq. (76). The final equation of the phase field vs. time has the following form:

$$\begin{aligned} \frac{\partial \phi_i}{\partial t} = & -\sum_{j=1}^n \frac{2M_{ij}^\phi}{n} \\ & \times \left[\sum_{k=1}^n \left\{ (W_{ik} - W_{jk}) \phi_k + \frac{1}{2} (a_{ik}^2 - a_{jk}^2) \nabla^2 \phi_k \right\} \right. \\ & \left. - \frac{8}{\pi} \sqrt{\phi_i \phi_j} \Delta E_{ij} \right]. \quad (86) \end{aligned}$$

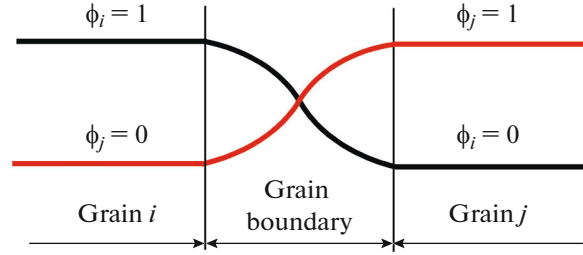


Fig. 8. Phase-field function change when moving from one grain to other.

The multiphase-field method was used to simulate dynamic recrystallization according to the following algorithm [104].

- (i) The initial polycrystalline structure was simulated according to [130].
- (ii) The initial dislocation density was selected.
- (iii) The dislocation density was found using the compression curve according to the Kocks–Mecking–Estrin model after increasing the strain rate by value $\Delta \epsilon$.

(iv) If the dislocation density exceeded the critical one, a recrystallization nucleus was created at the grain boundary.

(v) The grain growth process was calculated by solving the system of Eqs. (86).

Steps 3–5 were repeated until a required strain degree was reached. As a result, the authors determined the optimum parameters for Eqs. (86) and showed rather good agreement with the results calculated by the cellular automaton method [132]. This approach has demonstrated high efficiency in simulation of bainite and martensite formation during cooling of the two-phase DP600 austenite steel. It is shown that there is no need to specify the places of phase nucleation when taking into account elastic components in the calculation. The preferred planes for nucleation were the planes perpendicular to the martensite habitus. This method made it possible to simulate the formation of austenite, including its morphology and distribution of alloying elements, with high accuracy in martensitic Fe–9.6Ni–7.1Mn steel during its isothermal holding in the temperature range 510–600°C [133]. Kinoshita et al. applied this method to describe abnormal grain growth in a carburized layer of niobium-containing steel [134]. This method together with thermodynamical and diffusive calculations was also used to explain the abnormal plate divergence in pearlitic colonies during the austenite decomposition in the Fe–C–Mn steel [135].

Despite the rather complicated mathematical apparatus of the multiphase-field method implementation, it is quite promising for structural formation simulation due to the high diversity of factors affecting the phase field function.

CONCLUSIONS

(1) Physico-mathematical models based on the Johnson–Mehl–Avrami–Kolmogorov and Kocks–Mecking–Estrin equations and developed so far to describe structural evolution during hot plastic deformation allow one to predict structural parameters of metal materials with a high level of accuracy. The simple analytical regularities implemented by these models can be successfully integrated into modern computing systems for calculating industrial metal processing processes under pressure. However, a large number of unknown constants require a large number of mechanical tests and structural studies to build a comprehensive model that can take dynamic hardening, recovery, and recrystallization into consideration. As a result, the development of in-situ methods to determine microstructural parameters during hot plastic deformation and heat treatment is a promising trend in the research area.

(2) A significant theoretical foundation for calculating the kinetics of structural transformations during heating and cooling of steel, as well as during the decomposition of supersaturated solid solution, has been created. The models developed based on the theory of nucleation and growth demonstrate both high levels of accuracy in determining the volume fraction and size of phase transformation products, and the possibility of applying these models to determine mechanical properties.

(3) Numerical methods for calculating the structural evolution regularities are currently the most promising. Despite the minimum set of necessary experimental data, the cellular automaton, Monte Carlo, and multiphase-field methods demonstrate high accuracy in calculating recrystallization processes and phase transformations.

Thus, there is a comprehensive basis for the development of integrated adjustable models. These models offer end-to-end calculation of the complete heat and deformation treatment cycle of metal materials. There is a possibility of recursive optimization of technological parameters to achieve a desired structure. The key role in such models should be played by numerical calculation methods, which are the most universal and can be adjusted for use together with finite element simulation techniques.

FUNDING

This work was supported by the Russian Scientific Foundation (project no. 18-79-10153).

REFERENCES

- G. Shen, S. L. Semiatin, and R. Shivpuri, "Modeling microstructural development during the forging of Waspaloy," *Metall. Mater. Trans. A* **26**, 1795–1803 (1995).
- Q. M. Guo, D. F. Li, and S. L. Guo, "Microstructural models of dynamic recrystallization in hot-deformed inconel 625 superalloy," *Mater. Manuf. Process.* **27**, 990–995 (2012).
- M. G. Mecozzi, C. Bos, and J. Sietsma, "A mixed-mode model for the ferrite-to-austenite transformation in a ferrite/pearlite microstructure," *Acta Mater.* **88**, 302–313 (2015).
- E. Schoof, D. Schneider, N. Streichhan, T. Mittnacht, M. Selzer, and B. Nestler, "Multiphase-field modeling of martensitic phase transformation in a dual-phase microstructure," *Int. J. Solids Struct.* **134**, 181–194 (2018).
- Z. Li, Z. Wen, F. Su, R. Zhang, and Z. Zhou, "Modeling research on pearlite-to-austenite transformation in hypereutectoid steel containing Cr," *J. Alloys Compd.* **727**, 1050–1056 (2017).
- P. Hippchen, A. Lipp, H. Grass, P. Craighero, M. Fleischer, and M. Merklein, "Modelling kinetics of phase transformation for the indirect hot stamping process to focus on car body parts with tailored properties," *J. Mater. Process. Technol.* **228**, 59–67 (2016).
- F. Yin, L. Hua, H. Mao, X. Han, D. Qian, and R. Zhang, "Microstructural modeling and simulation for GCr15 steel during elevated temperature deformation," *Mater. Des.* **55**, 560–573 (2014).
- Z. Jin, K. Li, X. Wu, and H. Dong, "Modelling of microstructure evolution during thermoplastic deformation of steel by a finite element method," *Mater. Today Proc.* **2**, 460–465 (2015).
- A. M. Elwazri, E. Essadiqi, and S. Yue, "Kinetics of metadynamic recrystallization in microalloyed hypereutectoid steels," *ISIJ Int.* **44**, 744–752 (2004).
- V. V. Popov and I. I. Gorbachev, "Computer simulation for the prediction of phase composition and structure of low-alloyed steels with carbonitride hardening," *Phys. Met. Metallogr.* **119**, 1333–1337 (2018).
- I. I. Gorbachev, A. Y. Pasyukov, and V. V. Popov, "Simulation of the evolution of carbonitride particles of complex composition upon hot deformation of a low-alloyed steel," *Phys. Met. Metallogr.* **119**, 770–779 (2018).
- Ł. Łach, J. Nowak, and D. Svyetlichnyy, "The evolution of the microstructure in AISI 304L stainless steel during the flat rolling—modeling by frontal cellular automata and verification," *J. Mater. Process. Technol.* **255**, 488–499 (2018).
- M. S. Chen, W. Q. Yuan, Y. C. Lin, H. Bin. Li, and Z. H. Zou, "Modeling and simulation of dynamic recrystallization behavior for 42CrMo steel by an extended cellular automaton method," *Vacuum* **146**, 142–151 (2017).
- Y. Estrin and H. Mecking, "A unified phenomenological description of work hardening and creep based on one-parameter models," *Acta Metall.* **32**, 57–70 (1984).
- U. F. Kocks and H. Mecking, "Physics and phenomenology of strain hardening: The FCC case," *Prog. Mater. Sci.* **48**, 171–273 (2003).
- H. Mecking and U. F. Kocks, "Kinetics of flow and strain-hardening," *Acta Metall.* **29**, 1865–1875 (1981).

17. E. Nes, K. Marthinsen, and Y. Brechet, "On the mechanisms of dynamic recovery," *Scr. Mater.* **47**, 607–611 (2002).
18. E. Nes, "Modelling of work hardening and stress saturation in FCC metals," *Prog. Mater. Sci.* **41**, 129–193 (1997).
19. E. Nes and K. Marthinsen, "Modeling the evolution in microstructure and properties during plastic deformation of f.c.c.-metals and alloys—An approach towards a unified model," *Mater. Sci. Eng., A* **322**, 176–193 (2002).
20. J. G. Sevillano, "Flow stress and work hardening," in *Materials Science and Technology* (Wiley, 2006), pp. 21–88.
21. Y. Zhang, Q. Fan, X. Zhang, Z. Zhou, Z. Xia, and Z. Qian, "Avrami kinetic-based constitutive relationship for armco-type pure iron in hot deformation," *Metals (Basel)* **9**, 365 (2019).
22. J. Guo, M. Zhan, Y. Y. Wang, and P. F. Gao, "Unified modeling of work hardening and flow softening in two-phase titanium alloys considering microstructure evolution in thermomechanical processes," *J. Alloys Compd.* **767**, 34–45 (2018).
23. N. Haghdadi, D. Martin, and P. Hodgson, "Physically-based constitutive modelling of hot deformation behavior in a LDX 2101 duplex stainless steel," *Mater. Des.* **106**, 420–427 (2016).
24. W. A. Johnson and R. T. Mehl, "Reaction kinetics in processes of nucleation and growth," *Trans. AIME* **185**, 416–442 (1939).
25. M. Avrami, "Kinetics of phase change. II Transformation-time relations for random distribution of nuclei," *J. Chem. Phys.* **8**, 212–224 (1940).
26. A. N. Kolmogorov, "On the statistical theory of crystallization of metals," *Izv. Akad. Nauk SSSR, Ser. Mat.* **3**, 355–359 (1937).
27. H. J. McQueen, J. K. Solberg, N. Ryum, and E. Nes, "Evolution of flow stress in aluminium during ultra-high straining at elevated temperatures. Part II," *Philos. Mag. A* **60**, 473–485 (1989).
28. J. K. Solberg, H. J. McQueen, N. Ryum, and E. Nes, "Influence of ultra-high strains at elevated temperatures on the microstructure of aluminium. Part I," *Philos. Mag. A* **60**, 447–471 (1989).
29. T. Pettersen, B. Holmedal, and E. Nes, "Microstructure development during hot deformation of aluminium to large strains," *Metall. Mater. Trans. A* **34**, 2737–2744 (2003).
30. I. I. Gorbachev, A. Y. Pasyukov, and V. V. Popov, "Simulation of the effect of hot deformation on the austenite grain size of low-alloyed steels with carbonitride hardening," *Phys. Met. Metallogr.* **119**, 551–557 (2018).
31. C. Zener, "Private communication to C.S. Smith," *Trans. Am. Inst. Min. Eng.* **175**, 15 (1949).
32. T. Gladman, "On the theory of the effect of precipitate particles on grain growth in metals," *Proc. R. Soc. London. Ser. A* **294**, 298–309 (1966).
33. T. Nishizawa, I. Ohnuma, and K. Ishida, "Examination of the Zener relationship between grain size and particle dispersion," *Mater. Trans. JIM* **38**, 950–956 (1997).
34. I. I. Gorbachev, A. Y. Pasyukov, and V. V. Popov, "Prediction of the austenite-grain size of microalloyed steels based on the simulation of the evolution of carbonitride precipitates," *Phys. Met. Metallogr.* **116**, 1127–1134 (2015).
35. A. Y. Churyumov, A. V. Mikhailovskaya, A. D. Kotov, A. I. Bazlov, and V. K. Portnoi, "Development of mathematical models of superplasticity properties as a function of parameters of aluminum alloys of Al–Mg–Si system," *Phys. Met. Metallogr.* **114**, 272–278 (2013).
36. E. I. Poliak and J. J. Jonas, "A one-parameter approach to determining the critical conditions for the initiation of dynamic recrystallization," *Acta Mater.* **44**, 127–136 (1996).
37. M. Imran and M. Bambach, "A new model for dynamic recrystallization under hot working conditions based on critical dislocation gradients," *Procedia Eng.* **207**, 2107–2112 (2017).
38. W. P. Sun and E. B. Hawbolt, "Comparison between static and metadynamic recrystallization—An application to the hot rolling of steels," *ISIJ Int.* **37**, 1000–1009 (1997).
39. M. G. Khomutov, A. Y. Churyumov, A. V. Pozdnyakov, A. G. Voitenko, and A. A. Cheresheva, "Simulation of the kinetics of dynamic recrystallization of alloy KhN55MBYu-VD during hot deformation," *Met. Sci. Heat Treat.* **60**, 606–610 (2019).
40. S. Il. Kim, Y. Lee, and B. L. Jang, "Modeling of recrystallization and austenite grain size for AISI 316 stainless steel and its application to hot bar rolling," *Mater. Sci. Eng., A* **357**, 235–239 (2003).
41. A. Yu. Churyumov, A. V. Pozdnyakov, T. A. Churyumova, and V. V. Cheverikin, "Hot deformation behavior of heat-resistant austenitic AISI 310S steel. I. Modeling of the flow stress and dynamic recrystallization," *Chernye Met.* **8**, 48–55 (2020).
42. V. Dub, A. Churyumov, A. Rodin, S. Belikov, and A. Barbolin, "Prediction of grain size evolution for low alloyed steels," *Results Phys.* **8**, 584–586 (2018).
43. Á. Zufia and J. M. Llanos, "Mathematical simulation and controlled cooling in an EDC conveyor of a wire rod rolling mill," *ISIJ Int.* **41**, 1282–1288 (2001).
44. P. A. Manohar, K. Lim, A. D. Rollett, and Y. Lee, "Computational exploration of microstructural evolution in a medium C-Mn steel and applications to rod mill," *ISIJ Int.* **43**, 1421–1430 (2003).
45. M. Zhao, L. Huang, R. Zeng, H. Su, D. Wen, and J. Li, "In-situ observations and modeling of metadynamic recrystallization in 300M steel," *Mater. Charact.* **159**, 109997 (2020).
46. D. G. He, Y. C. Lin, and L. H. Wang, "Microstructural variations and kinetic behaviors during metadynamic recrystallization in a nickel base superalloy with pre-precipitated δ phase," *Mater. Des.* **165**, 107584 (2019).
47. D. Dong, F. Chen, and Z. Cui, "Investigation on metadynamic recrystallization behavior in SA508-III steel during hot deformation," *J. Manuf. Process.* **29**, 18–28 (2017).
48. J. Majta, J. G. Lenard, and M. Pietrzyk, "Modelling the evolution of the microstructure of a Nb steel," *ISIJ Int.* **36**, 1094–1102 (1996).

49. F. Chen, Z. Cui, D. Sui, and B. Fu, "Recrystallization of 30Cr2Ni4MoV ultra-super-critical rotor steel during hot deformation. Part III: Metadynamic recrystallization," *Mater. Sci. Eng., A* **540**, 46–54 (2012).
50. B. Ma, Y. Peng, B. Jia, and Y. F. Liu, "Static recrystallization kinetics model after hot deformation of low-alloy steel Q345B," *J. Iron Steel Res. Int.* **17**, 61–66 (2010).
51. M. Zhao, L. Huang, R. Zeng, D. Wen, H. Su, and J. Li, "In-situ observations and modeling of static recrystallization in 300 M steel," *Mater. Sci. Eng., A* **765**, 138300 (2019).
52. N. Nakata and M. Militzer, "Modelling of microstructure evolution during hot rolling of a 780 MPa high strength steel," *ISIJ Int.* **45**, 82–90 (2005).
53. Y. Yogo, K. Tanaka, and K. Nakanishi, "In-situ observation of grain growth of steel at high temperature," *Mater. Trans.* **50**, 280–285 (2009).
54. M. Dubois, M. Militzer, A. Moreau, and J. F. Busière, "New technique for the quantitative real-time monitoring of austenite grain growth in steel," *Scr. Mater.* **42**, 867–874 (2000).
55. M. Toozandehjani, K. A. Matori, F. Ostovan, F. Mustapha, N. I. Zahari, and A. Oskoueian, "On the correlation between microstructural evolution and ultrasonic properties: a review," *J. Mater. Sci.* **50**, 2643–2665 (2015).
56. T. Garcin, J. H. Schmitt, and M. Militzer, "In-situ laser ultrasonic grain size measurement in superalloy INCONEL 718," *J. Alloys Compd.* **670**, 329–336 (2016).
57. L. P. Karjalainen, "Stress relaxation method for investigation of softening kinetics in hot deformed steels," *Mater. Sci. Technol.* **11**, 557–565 (1995).
58. L. Cheng, H. Chang, B. Tang, H. Kou, and J. Li, "Characteristics of metadynamic recrystallization of a high Nb containing TiAl alloy," *Mater. Lett.* **92**, 430–432 (2013).
59. B. Hodgson and R. K. Gibbs, "A mathematical hot rolled C-Mn model to predict and microalloyed the mechanical properties of steels," *ISIJ Int.* **32**, 1329–1338 (1992).
60. F. Liu, F. Sommer, C. Bos, and E. J. Mittemeijer, "Analysis of solid state phase transformation kinetics: Models and recipes," *Int. Mater. Rev.* **52**, 193–212 (2007).
61. N. Li, J. Lin, D. S. Balint, and T. A. Dean, "Modelling of austenite formation during heating in boron steel hot stamping processes," *J. Mater. Process. Technol.* **237**, 394–401 (2016).
62. M. Bellavoine, M. Dumont, M. Dehmas, A. Stark, N. Schell, J. Drillet, V. Hébert, and P. Maugis, "Ferrite recrystallization and austenite formation during annealing of cold-rolled advanced high-strength steels: In situ synchrotron X-ray diffraction and modeling," *Mater. Charact.* **154**, 20–30 (2019).
63. H. Li, K. Gai, L. He, C. Zhang, H. Cui, and M. Li, "Non-isothermal phase-transformation kinetics model for evaluating the austenization of 55CrMo steel based on Johnson-Mehl-Avrami equation," *Mater. Des.* **92**, 731–741 (2016).
64. M. P. De Andres and M. Carsí, "Hardenability: an alternative to the use of grain size as calculation parameter," *J. Mater. Sci.* **22**, 2707–2716 (1987).
65. I. Tamura, H. Sekine, and T. Tanaka, *Thermomechanical Processing of High-Strength Low-Alloy Steels* (Butterworth-Heinemann, 1988).
66. S. Kamamoto, T. Nishimori, and S. Kinoshita, "Analysis of residual stress and distortion resulting from quenching in large low-alloy steel shafts," *Mater. Sci. Technol.* **1**, 798–804 (1985).
67. S. J. Johns and H. K. D. H. Bhadeshia, "Kinetics of the Simultaneous Decomposition of Austenite into Several Transformation Products," *Acta Metall. Mater.* **45**, 2911–2920 (1997).
68. C. Zener, "Kinetics of the decomposition of austenite," *Trans. AIME* **167**, 550–595 (1946).
69. M. Hillert, "The role of interfacial energy during solid-state phase transformations," *Jernkontorets Ann.* **141**, 757–789 (1957).
70. M. Li Victor, D. V. Niebuhr, L. L. Meekisho, and D. G. Atteridge, "A computational model for the prediction of steel hardenability," *Metall. Mater. Trans. B* **29**, 661–672 (1998).
71. D. P. Koistinen and R. E. Marburger, "A general equation prescribing the extent of the austenite-martensite transformation in pure iron-carbon alloys and plain carbon steels," *Acta Metall.* **7**, 59–60 (1959).
72. S. J. Lee and Y. K. Lee, "Finite element simulation of quench distortion in a low-alloy steel incorporating transformation kinetics," *Acta Mater.* **56**, 1482–1490 (2008).
73. H. Zhao, X. Hu, J. Cui, and Z. Xing, "Kinetic model for the phase transformation of high-strength steel under arbitrary cooling conditions," *Met. Mater. Int.* **25**, 381–395 (2019).
74. G. Venturato, S. Bruschi, A. Ghiotti, and X. Chen, "Numerical modeling of the 22MnB₅ formability at high temperature," *Procedia Manuf.* **29**, 428–434 (2019).
75. S. J. Lee, E. J. Pavlina, and C. J. Van Tyne, "Kinetics modeling of austenite decomposition for an end-quenched 1045 steel," *Mater. Sci. Eng., A* **527**, 3186–3194 (2010).
76. W. Chen, L. Xu, L. Zhao, Y. Han, H. Jing, Y. Zhang, and Y. Li, "Thermo-mechanical-metallurgical modeling and validation for ferritic steel weldments," *J. Constr. Steel Res.* **166**, 105948 (2020).
77. Q. Wang, X. S. Liu, P. Wang, X. Xiong, and H. Y. Fang, "Numerical simulation of residual stress in 10Ni₅CrMoV steel weldments," *J. Mater. Process. Technol.* **240**, 77–86 (2017).
78. M. J. Starink, C. Y. Zahra, and A. M. Zahra, "Analysis of precipitation in Al-based alloys using a novel model for nucleation and growth reactions," *J. Therm. Anal. Calorim.* **51**, 933–942 (1998).
79. O. R. Myhr, Grong, H. G. Fjær, and C. D. Marioara, "Modelling of the microstructure and strength evolution in al-mg-si alloys during multistage thermal processing," *Acta Mater.* **52**, 4997–5008 (2004).
80. R. Wagner, R. Kampmann, and P. W. Voorhees, "Homogeneous second-phase precipitation," in *Mater. Sci. Technol.* (2013), pp. 309–407.

81. A. Simar, Y. Bréchet, B. de Meester, A. Denquin, and T. Pardoen, "Sequential modeling of local precipitation, strength and strain hardening in friction stir welds of an aluminum alloy 6005A-T6," *Acta Mater.* **55**, 6133–6143 (2007).
82. M. Perez, M. Dumont, and D. Acevedo-Reyes, "Implementation of classical nucleation and growth theories for precipitation," *Acta Mater.* **56**, 2119–2132 (2008).
83. J. da Costa Teixeira, D. G. Cram, L. Bourgeois, T. J. Bastow, A. J. Hill, and C. R. Hutchinson, "On the strengthening response of aluminum alloys containing shear-resistant plate-shaped precipitates," *Acta Mater.* **56**, 6109–6122 (2008).
84. D. Bardel, M. Perez, D. Nelias, A. Deschamps, C. R. Hutchinson, D. Maissonnette, T. Chaise, J. Garnier, and F. Bourlier, "Coupled precipitation and yield strength modelling for non-isothermal treatments of a 6061 aluminium alloy," *Acta Mater.* **62**, 129–140 (2014).
85. J. D. Robson and P. B. Prangnell, "Dispersoid precipitation and process modelling in zirconium containing commercial aluminum alloys," *Acta Mater.* **49**, 599–613 (2001).
86. J. W. Christian, *The Theory of Transformations in Metals and Alloys* (Pergamon, 2002), 1st ed.
87. N. Saunders, "Calculated stable and metastable phase equilibria in Al–Li–Zr alloys," *Z. Met.* **80**, 894–903 (1989).
88. D. A. Porter and K. E. Easterling, *Phase Transformations in Metals and Alloys* (Chapman & Hall, Ed., 1992).
89. J. D. Robson, M. J. Jones, and P. B. Prangnell, "Extension of the N-model to predict competing homogeneous and heterogeneous precipitation in Al–Sc alloys," *Acta Mater.* **51**, 1453–1468 (2003).
90. J. D. Robson, "A new model for prediction of dispersoid precipitation in aluminium alloys containing zirconium and scandium," *Acta Mater.* **52**, 1409–1421 (2004).
91. E. Clouet, A. Barbu, L. Laé, and G. Martin, "Precipitation kinetics of Al₃Zr and Al₃Sc in aluminum alloys modeled with cluster dynamics," *Acta Mater.* **53**, 2313–2325 (2005).
92. V. S. Zolotarevskii, A. V. Pozdnyakov, and A. Y. Churyumov, "Search for promising compositions for developing new multiphase casting alloys based on Al–Zn–Mg matrix using thermodynamic calculations and mathematic simulation," *Phys. Met. Metallogr.* **115**, 286–294 (2014).
93. V. S. Zolotarevskii, A. V. Pozdnyakov, and A. Y. Churyumov, "Search for promising compositions for developing new multiphase casting alloys based on Al–Cu–Mg matrix using thermodynamic calculations and mathematic simulation," *Phys. Met. Metallogr.* **113**, 1052–1060 (2012).
94. D. S. Svyetlichnyy, J. Nowak, and Ł. Łach, "Modeling of recrystallization with recovery by frontal cellular automata," in *Proceedings of the Lecture Notes in Computer Science (including subseries Lecture Notes in Artificial Intelligence and Lecture Notes in Bioinformatics)* (2012), pp. 494–503.
95. O. Seppälä, A. Pohjonen, A. Kaijalainen, J. Larkiola, and D. Porter, "Simulation of bainite and martensite formation using a novel cellular automata method," *Procedia Manuf.* **15**, 1856–1863 (2018).
96. S. Kundu, M. Dutta, S. Ganguly, and S. Chandra, "Prediction of phase transformation and microstructure in steel using cellular automaton technique," *Scr. Mater.* **50**, 891–895 (2004).
97. J. Zhang, Z. Li, K. Wen, S. Huang, X. Li, H. Yan, L. Yan, H. Liu, Y. Zhang, and B. Xiong, "Simulation of dynamic recrystallization for an Al–Zn–Mg–Cu alloy using cellular automaton," *Prog. Nat. Sci. Mater. Int.* **29**, 477–484 (2019).
98. M. Sitko, M. Pietrzyk, and L. Madej, "Time and length scale issues in numerical modelling of dynamic recrystallization based on the multi space cellular automata method," *J. Comput. Sci.* **16**, 98–113 (2016).
99. S. Hore, S. K. Das, S. Banerjee, and S. Mukherjee, "Computational modelling of static recrystallization and two dimensional microstructure evolution during hot strip rolling of advanced high strength steel," *J. Manuf. Process.* **17**, 78–87 (2015).
100. M. A. Steiner, R. J. McCabe, E. Garlea, and S. R. Agnew, "Monte Carlo modeling of recrystallization processes in α -uranium," *J. Nucl. Mater.* **492**, 74–87 (2017).
101. D. Molnar, C. Niedermeier, A. Mora, P. Binkele, and S. Schmauder, "Activation energies for nucleation and growth and critical cluster size dependence in JMAK analyses of kinetic Monte-Carlo simulations of precipitation," *Continuum Mech. Thermodyn.* **24**, 607–617 (2012).
102. J. Rasti, "Study of the grain size distribution during preheating period prior to the hot deformation in AISI 316L austenitic stainless steel," *Phys. Met. Metallogr.* **120**, 584–592 (2019).
103. O. I. Gorbatov, Y. N. Gornostyrev, P. A. Korzhavyi, and A. V. Ruban, "Ab initio modeling of decomposition in iron based alloys," *Phys. Met. Metallogr.* **117**, 1293–1327 (2016).
104. T. Takaki, T. Hirouchi, Y. Hisakuni, A. Yamanaka, Y. Tomita, "Multi-phase-field model to simulate microstructure evolutions during dynamic recrystallization," *Mater. Trans.* **49**, 2559–2565 (2008).
105. J. Zhang, C. W. Zheng, and D. Z. Li, "A multi-phase field model for static recrystallization of hot deformed austenite in a C–Mn steel," *Acta Metall. Sin. (English Lett)* **31**, 208–215 (2018).
106. K. G. F. Janssens, "An introductory review of cellular automata modeling of moving grain boundaries in polycrystalline materials," *Math. Comput. Simul.* **80**, 1361–1381 (2010).
107. L. Sieradzki and L. Madej, "A perceptive comparison of the cellular automata and Monte Carlo techniques in application to static recrystallization modeling in polycrystalline materials," *Comput. Mater. Sci.* **67**, 156–173 (2013).
108. H. Hallberg, "Approaches to modeling of recrystallization," *Metals (Basel)* **1**, 16–48 (2011).
109. X. Song and M. Rettenmayr, "Modeling recrystallization in a material containing fine and coarse particles," *Comput. Mater. Sci.* **40**, 234–245 (2007).

110. Y. C. Lin, Y. X. Liu, M. S. Chen, M. H. Huang, X. Ma, and Z. L. Long, "Study of static recrystallization behavior in hot deformed Ni-based superalloy using cellular automaton model," *Mater. Des.* **99**, 107–114 (2016).
111. R. D. Doherty, D. A. Hughes, F. J. Humphreys, J. J. Jonas, D. Jensen Juul, M. E. Kassner, W. E. King, T. R. McNelley, H. J. McQueen, and A. D. Rollett, "Current issues in recrystallization: A review," *Mater. Sci. Eng., A* **238**, 219–274 (1997).
112. Y. X. Liu, Y. C. Lin, and Y. Zhou, "2D cellular automaton simulation of hot deformation behavior in a Ni-based superalloy under varying thermal-mechanical conditions," *Mater. Sci. Eng., A* **691**, 88–99 (2017).
113. L. Madej, M. Sitko, K. Perzynski, L. Sieradzki, K. Radwanski, and R. Kuziak, "Multi scale cellular automata and finite element based model for cold deformation and annealing of a ferritic-pearlitic microstructure," *Multiscale Mater. Model.* **77**, 235–254 (2016).
114. R. Ding and Z. X. Guo, "Coupled quantitative simulation of microstructural evolution and plastic flow during dynamic recrystallization," *Acta Mater.* **49**, 3163–3175 (2001).
115. F. Chen, Z. Cui, J. Liu, W. Chen, and S. Chen, "Mesoscale simulation of the high-temperature austenitizing and dynamic recrystallization by coupling a cellular automaton with a topology deformation technique," *Mater. Sci. Eng., A* **527**, 5539–5549 (2010).
116. F. Chen, K. Qi, Z. Cui, and X. Lai, "Modeling the dynamic recrystallization in austenitic stainless steel using cellular automaton method," *Comput. Mater. Sci.* **83**, 331–340 (2014).
117. Y. X. Liu, Y. C. Lin, H. Bin. Li, D. X. Wen, X. M. Chen, and M. S. Chen, "Study of dynamic recrystallization in a Ni-based superalloy by experiments and cellular automaton model," *Mater. Sci. Eng., A* **626**, 432–440 (2015).
118. F. Sun, D. Q. Zhang, L. Cheng, P. Zheng, D. M. Liao, and B. Zhu, "Microstructure evolution modeling and simulation for dynamic recrystallization of Cr₁₂MoV die steel during hot compression based on real metallographic image," *Met. Mater. Int.* **25**, 966–981 (2019).
119. C. Zhang, L. Zhang, Q. Xu, Y. Xia, and W. Shen, "The kinetics and cellular automaton modeling of dynamic recrystallization behavior of a medium carbon Cr–Ni–Mo alloyed steel in hot working process," *Mater. Sci. Eng., A* **678**, 33–43 (2016).
120. H. Zhang, J. Wang, Q. Chen, D. Shu, C. Wang, G. Chen, and Z. Zhao, "Study of dynamic recrystallization behavior of T2 copper in hot working conditions by experiments and cellular automaton method," *J. Alloys Compd.* **784**, 1071–1083 (2019).
121. X. Li, X. Li, H. Zhou, X. Zhou, F. Li, and Q. Liu, "Simulation of dynamic recrystallization in AZ80 magnesium alloy using cellular automaton," *Comput. Mater. Sci.* **140**, 95–104 (2017).
122. N. Yazdipour and P. D. Hodgson, "Modelling post-deformation softening kinetics of 304 austenitic stainless steel using cellular automata," *Comput. Mater. Sci.* **54**, 56–65 (2012).
123. Y. J. Lan, D. Z. Li, and Y. Y. Li, "Modeling austenite decomposition into ferrite at different cooling rate in low-carbon steel with cellular automaton method," *Acta Mater.* **52**, 1721–1729 (2004).
124. Y. J. Lan, D. Z. Li, and Y. Y. Li, "Mesoscale simulation of ferrite transformation from deformed austenite during continuous cooling in a C–Mn steel using a cellular automaton method," *Comput. Mater. Sci.* **32**, 147–155 (2005).
125. M. Militzer, R. Pandi, and E. B. Hawbolt, "Ferrite nucleation and growth during continuous cooling," *Metall. Mater. Trans. A* **27**, 1547–1556 (1996).
126. B. J. Yang, L. Chuzhoy, and M. L. Johnson, "Modeling of reaustenitization of hypoeutectoid steels with cellular automaton method," *Comput. Mater. Sci.* **41**, 186–194 (2007).
127. X. Yu and S. Chen, "A simulation of Cr depletion in austenitic stainless steel with cellular automaton," *Comput. Mater. Sci.* **45**, 899–904 (2009).
128. S. Hore, S. K. Das, S. Banerjee, and S. Mukherjee, "A multiscale coupled Monte Carlo model to characterize microstructure evolution during hot rolling of Mo-TRIP steel," *Acta Mater.* **61**, 7251–7259 (2013).
129. M. Kazeminezhad, "On the modeling of the static recrystallization considering the initial grain size effects," *Mater. Sci. Eng., A* **486**, 202–207 (2008).
130. C. E. Krill and L. Q. Chen, "Computer simulation of 3-D grain growth using a phase-field model," *Acta Mater.* **50**, 3057–3073 (2002).
131. I. Steinbach and F. Pezzolla, "A generalized field method for multiphase transformations using interface fields," *Phys. D* **134**, 385–393 (1999).
132. G. Kugler and R. Turk, "Modeling the dynamic recrystallization under multi-stage hot deformation," *Acta Mater.* **52**, 4659–4668 (2004).
133. X. Zhang, G. Shen, C. Li, and J. Gu, "Phase-field simulation of austenite reversion in a Fe–9.6Ni–7.1Mn (at %) martensitic steel governed by a coupled diffusional/displacive mechanism," *Mater. Des.* **188**, 108426 (2020).
134. T. Kinoshita and M. Ohno, "Phase-field simulation of abnormal grain growth during carburization in Nb-added steel," *Comput. Mater. Sci.* **177**, 109558 (2020).
135. L. T. Mushongera, P. G. K. Amos, B. Nestler, and K. Ankit, "Phase-field simulations of pearlitic divergence in Fe–C–Mn steels," *Acta Mater.* **150**, 78–87 (2018).

Translated by T. Gapontseva